

## Boosting the Radiosensitizing and Photothermal Performance of CuSe Nanocrystals for Synergetic Radiophotothermal Therapy of Orthotopic Breast Cancer

Qian Huang, Shaohua Zhang, Hao Zhang, Yaobao Han,  
Hanghang Liu, Feng Ren, Qiao Sun, Zhen Li, and Mingyuan Gao

ACS Nano, Just Accepted Manuscript • DOI: 10.1021/acsnano.8b06795 • Publication Date (Web): 01 Feb 2019

Downloaded from <http://pubs.acs.org> on February 4, 2019

### Just Accepted

"Just Accepted" manuscripts have been peer-reviewed and accepted for publication. They are posted online prior to technical editing, formatting for publication and author proofing. The American Chemical Society provides "Just Accepted" as a service to the research community to expedite the dissemination of scientific material as soon as possible after acceptance. "Just Accepted" manuscripts appear in full in PDF format accompanied by an HTML abstract. "Just Accepted" manuscripts have been fully peer reviewed, but should not be considered the official version of record. They are citable by the Digital Object Identifier (DOI®). "Just Accepted" is an optional service offered to authors. Therefore, the "Just Accepted" Web site may not include all articles that will be published in the journal. After a manuscript is technically edited and formatted, it will be removed from the "Just Accepted" Web site and published as an ASAP article. Note that technical editing may introduce minor changes to the manuscript text and/or graphics which could affect content, and all legal disclaimers and ethical guidelines that apply to the journal pertain. ACS cannot be held responsible for errors or consequences arising from the use of information contained in these "Just Accepted" manuscripts.

# Boosting the Radiosensitizing and Photothermal Performance of Cu<sub>2-x</sub>Se Nanocrystals for Synergetic Radiophotothermal Therapy of Orthotopic Breast Cancer

*Qian Huang, Shaohua Zhang, Hao Zhang, Yaobao Han, Hanghang Liu, Feng Ren, Qiao Sun, Zhen Li\*, Mingyuan Gao*

Center for Molecular Imaging and Nuclear Medicine, State Key Laboratory of Radiation Medicine and Protection, School for Radiological and Interdisciplinary Sciences (RAD-X), Soochow University, Collaborative Innovation Center of Radiation Medicine of Jiangsu Higher Education Institutions  
Suzhou 215123, China

## ABSTRACT

The small difference between tumor and normal tissues in their responses to ionizing radiation has been a significant issue for radiotherapy of tumors. Herein, we report that dumbbell-shaped heterogeneous copper selenide-gold nanocrystals can serve as an efficient radiosensitizer for enhanced radiotherapy. The mean lethal dose of X-rays to 4T1 tumor cells can be drastically decreased about 40%, *i.e.*, decreasing from 1.81 Gy to 1.10 Gy after culture with heterostructures. Due to the synergetic effect of heterostructures, the dose of X-rays is also much lower than those obtained from mixture of Cu<sub>2-x</sub>Se + Au nanoparticles (1.78 Gy), Cu<sub>2-x</sub>Se nanoparticles (1.72 Gy) and Au nanoparticles (1.50 Gy), respectively. We demonstrate that the sensitivity enhancement ratio of Cu<sub>2-x</sub>Se nanoparticles was significantly improved 45% (*i.e.*, from 1.1 to 1.6) after the formation of heterostructures with gold. We also show that the hetero-nanocrystals exhibit an enhanced photothermal conversion efficiency, due to the

1  
2  
3  
4 synergetic interactions of localized surface plasmon resonance. These properties highly  
5 feature them as a multimodal imaging contrast agent (particular for photoacoustic  
6 imaging, computed tomography imaging, and single photon emission computed  
7 tomography after labeled with radioisotopes) and as a radiosensitizer for imaging  
8 guided synergetic radiophotothermal treatment of cancer. The research provides  
9 insights for engineering low-Z nanomaterials with high Z elements to form hetero-  
10 nanostructures with enhanced synergetic performance for tumor theranostics.  
11  
12  
13  
14  
15  
16  
17

18 **KEYWORDS:** heterogeneous nanoparticles, radiosensitizer, radiotherapy,  
19 photothermal therapy, multimodal imaging  
20  
21  
22  
23  
24  
25  
26  
27  
28  
29  
30  
31  
32  
33  
34  
35  
36  
37  
38  
39  
40  
41  
42  
43  
44  
45  
46  
47  
48  
49  
50  
51  
52  
53  
54  
55  
56  
57  
58  
59  
60

Radiotherapy (RT) is one of the most important and effective methods for the treatment of solid tumors, as more than half of tumor patients would receive RT during treatment.<sup>1</sup> RT mainly uses high energy radiation (*e.g.*, X-rays or  $\gamma$ -rays) to target cancerous tissues, and then directly or indirectly damages the deoxyribonucleic acid (DNA) of cells, leading to apoptosis and death of irradiated cells.<sup>2, 3</sup> Despite its various advantages, the small difference between tumor and normal tissues in their responses to ionizing radiation leads to the difficulty in successfully curing solid cancers by RT alone without injury to normal tissues.<sup>4-6</sup> Therefore, how to improve the efficacy of RT remains a significant issue for cancer treatment.<sup>7</sup>

To maximize the radiosensitivity of tumor tissue to radiations and minimize the damage of radiations to normal tissue simultaneously, a number of high-Z elements (*e.g.*, gold, bismuth, wolfram, platinum, gadolinium ) based nanomaterials have been exploited as radiosensitizers,<sup>8-16</sup> which can penetrate into tumor *via* the enhanced permeability and retention (EPR) effect.<sup>17, 18</sup> These nanomaterials could be a generation of theranostic agents for multimodal imaging guided multiple therapy, by rationally integrating computed tomography (CT) imaging, photoacoustic (PA) imaging, and magnetic resonance imaging (MRI) with versatile therapeutic approaches including radiotherapy, photothermal therapy (PTT), and photodynamic therapy (PDT).<sup>19-23</sup>

Previous research has demonstrated that, with the assistance of these nanoagents, combinations of RT with other therapies could significantly improve its therapeutic efficacy.<sup>24-28</sup> One of the optimal portfolios is the combination of RT with PTT, which could successfully ablate tumor cells without metastasis and recurrence. In this context,

Au-,<sup>9, 29</sup> Bi-,<sup>11, 30</sup> and W-<sup>13, 31</sup> based nanomaterials could be an ideal choice due to their high-mass energy absorption coefficients, high photothermal conversion efficiency, excellent biocompatibility, and easy modification.

From the perspective of interactions between nanomaterials and X-rays, the photoelectric effect and Compton scattering are strongly dependent on the atomic number ( $Z$ ) and the photon energy. The material with high  $Z$  has a pronounced photoelectric effect and small Compton scattering when irradiated with high photon energy. In contrast, the material with low  $Z$  exhibits the strong Compton scattering and weak photoelectric effect when irradiated with low photon energy. In addition to above mentioned high  $Z$ -element based nanoagents, some light elements based nanomaterials also show strong attenuation to low energy X-rays and high photothermal conversion efficiency. For example, ultra-small  $\text{Cu}_{2-x}\text{Se}$  and  $\text{CuFeSe}_2$  nanocrystals exhibited stronger attenuation of X-rays and better performance in CT imaging than the clinically used iopromide.<sup>32-34</sup> These properties highlight their promise in imaging guided radiophotothermal therapy of cancer.

To maximally improve the performance of both low- and high- $Z$  elements based nanomaterials in a wide range of X-rays for multimodal imaging and therapy, they have been engineered by diverse approaches,<sup>35-40</sup> in which formation of their heterostructures has attracted considerable interest, because the resultant heterostructures not only exhibit the characteristics of the individual components, but also feature synergetic properties.<sup>41, 42</sup> For example, both core-shell  $\text{Au}@\text{Cu}_{2-x}\text{E}$  and dumbbell-shaped  $\text{Cu}_{2-x}\text{E}-\text{Au}$  ( $\text{E} = \text{S}, \text{Se}$ ) nanoparticles showed a higher photothermal conversion efficiency than

individual components,<sup>43-47</sup> which was attributed to their synergetic near infrared stronger localized surface plasmon resonance (LSPR). The enhanced photothermal conversion property makes them very attractive in the aspects of PA imaging and PTT.

The  $\text{Cu}_{2-x}\text{E-Au}$  ( $\text{E} = \text{S}, \text{Se}$ ) hetero-nanostructures are also expected to exhibit stronger attenuation of X-rays and a larger attenuation coefficient in comparison with copper chalcogenide and gold nanoparticles, because of the synergetic interactions of X-rays with multiple elements in the heterostructures. There are no reports, however, on their radio-enhancement and important application in radiotherapy.<sup>48, 49</sup> Moreover, the currently available  $\text{Cu}_{2-x}\text{E-Au}$  nanostructures were prepared either in organic solvents at high temperature or in aqueous solutions with use of reducing agents.<sup>43, 48,</sup>

50

In this article, dumbbell-shaped heterogeneous copper selenide-gold nanoparticles (CSA) were prepared by simply mixing  $\text{Cu}_{2-x}\text{Se}$  nanoparticles with  $\text{HAuCl}_4$  in aqueous solution under ambient conditions, which is completely different from previous reports as no reducing agent was used. The thus-formed CSA heterostructures exhibit significant enhancement of radiosensitization in comparison with  $\text{Cu}_{2-x}\text{Se}$  nanocrystals (CS), gold (Au) nanoparticles, and their mixture, leading to the excellence in damaging DNA strands of tumor cells. Our CSA nanoparticles also display a higher photothermal conversion efficiency than CS nanoparticles due to the synergetic interactions with Au nanoparticles. The CSA heterostructures were modified with dimercaptopoly(ethylene glycol) (HS-PEG-SH), labeled with radioactive  $^{99\text{m}}\text{Tc}$  and demonstrated to be a radiosensitizer, photothermal transducer for combined radiophotothermal therapy of

cancer, and as well as a contrast agent for multimodal imaging (*i.e.*, PA imaging, CT imaging, and single photon emission computed tomography (SPECT)) (Scheme 1).

## RESULTS AND DISCUSSION

The CSA heterostructures were synthesized in two steps in an aqueous solution under ambient conditions. First, the  $\text{Cu}_{2-x}\text{Se}$  nanocrystals (CS) were obtained *via* a modified protocol reported elsewhere.<sup>51, 52</sup> Briefly, selenium (Se) nanoparticles were obtained by reduction of  $\text{SeO}_2$  with Vitamin C. The resultant Se nanoparticles served as sacrificial templates and reacted with  $\text{Cu}^+$  ions to form copper selenide nanoparticles. The formed copper selenide nanoparticles were slowly oxidized by air and eventually transformed into CS nanoparticles, which were purified by filtration and centrifugation. Second, an  $\text{HAuCl}_4$  solution was quickly poured into the solution of purified CS nanoparticles under magnetic stirring, and reacted for 3 h to form heterostructured nanoparticles.

Transmission electron microscopy (TEM) was used to characterize the size and morphology of resulting CS and CSA nanoparticles. As shown in **Figure 1a**, the CS nanoparticles are spherical and have a mean size of  $17.6 \pm 1.4$  nm (**Figure S1a** in the Supporting Information). After reaction with  $\text{HAuCl}_4$ , the dumb-bell shaped heterostructures are clearly observed (**Figure 1b**), in which the larger spherical parts have a similar size ( $17.5 \pm 1.4$  nm, **Figure S1b**) to that of CS nanoparticles, which indicates that they are copper selenide, and the smaller spherical parts have a size of  $7.6 \pm 1.4$  nm (**Figure S1c**) and could be assigned as formed Au nanoparticles. In addition, there is a small portion of heterostructures having two or three small nanoparticles

attached to a large one.

The high-resolution TEM (HRTEM), elemental mapping and energy dispersive spectrometer (EDS) were used to further characterize the resultant heterostructures [Figure 1(c-d) and Figure S(2-3)]. The lattice spacings of large particles and small ones in the heterostructures were measured to be 0.203 nm and 0.235 nm, which are well matched with those of copper selenide and gold, respectively. The results clearly demonstrate that the hetero-nanostructures consist of copper selenide and gold, which is further confirmed by their elemental mapping and dark field images. The formation of CSA heterostructures is attributed to spontaneous redox reactions at the interface between the  $\text{Cu}_{2-x}\text{Se}$  nanoparticles and  $\text{HAuCl}_4$ , due to the much smaller redox potential of  $\text{Cu}^{2+}/\text{Cu}^+$  ( $E_{(\text{Cu}^{2+}/\text{Cu}^+)} = 0.153 \text{ V}$ ) than that of  $\text{Au}^{3+}/\text{Au}$  (*i.e.*  $E_{(\text{Au}^{3+}/\text{Au})} = 1.498 \text{ V}$ ). In addition, the surface defects of CS nanoparticles and the large lattice mismatch between copper selenide and gold are also responsible for the formation of dumbbell-shaped, rather than core-shell heterostructures.

The X-ray powder diffraction (XRD) patterns of as-prepared CS and CSA nanoparticles are compared in Figure 1e. All the characteristic diffraction peaks of CS nanoparticles match well with those of cubic berzelianite ( $\text{Cu}_{2-x}\text{Se}$ , JCPDS No. 06-0680). The strong peaks from CSA hetero-nanoparticles are indexed to be the characteristic peaks of cubic gold (Au, JCPDS No. 04-0784), and the weak ones, which could be ascribed to copper selenide in the heterostructures, are slightly blue-shifted in comparison with those of the CS nanoparticles. In addition, the strong LSPR of CS nanocrystals (Figure 1f) was weakened after the formation of CSA heterostructures,



accompanied with the appearance of characteristic LSPR of Au nanoparticles in the range of 500-550 nm.

To reveal the spontaneous redox reactions between the CS nanoparticles and  $\text{HAuCl}_4$ , the changes in the valence states of elements in the CS and CSA nanoparticles were examined with X-ray photoelectron spectroscopy (XPS, **Figure S4**). The binding energy of Cu 2p orbital in the CS nanoparticles shows the majority of  $\text{Cu}^+$  ions, most which were oxidized into  $\text{Cu}^{2+}$  ions in the formation of CSA heterostructures. The characteristic binding energy of Au 4f at 83.5 eV and 87.1 eV is attributed to  $\text{Au}^0$ . The atomic ratios in CS and CSA nanoparticles were determined by inductively coupled plasma – optical emission spectroscopy (ICP-OES) (**Table S1**). The atomic ratio of Cu/Se in the CS nanoparticles is 1.86, which illustrates their characteristics of copper deficiency. The atomic ratio of Cu/Se/Au within CSA heterostructures is 1:2.26:1.75. The decrease in the Cu/Se ratio in the CSA nanoparticles also supports the reduction of  $\text{Au}^{3+}$  by CS nanoparticles.

All the above results demonstrate the spontaneous formation of CSA hetero-nanostructures after the addition of  $\text{HAuCl}_4$  solution into CS nanoparticle solution. To improve the colloidal stability and biocompatibility of CSA nanoparticles, they were modified with HS-PEG-SH. The zeta potential of unmodified CSA nanoparticles (+3.25 mV, **Figure S5a**) is lower than that of CS nanoparticles (+9.00 mV), and it changed to -0.20 mV after modification with HS-PEG-SH. The slight change in zeta potential indicates the successful surface modification, which is also supported by the variation of their hydrodynamic size from 24.2 nm to 37.9 nm (**Figure S5b**). The

PEGylated CSA nanoparticles can be well dispersed in aqueous solution, saline solution (0.9 wt% NaCl), phosphate buffered saline (PBS) solution, and 10% fetal bovine serum (FBS) solution. The negligible change in their hydrodynamic size over 5 days suggests their excellent stability in these media (**Figure S6**) after surface modification.

Previous reports have demonstrated that nanoparticles with pronounced near-infrared LSPR or broad absorbance can efficiently convert near-infrared light into heat.<sup>32, 33, 41</sup> To demonstrate their performance difference in photothermal conversion, their extinction coefficients were obtained by measuring the UV-Vis-NIR absorbance of different concentrations of PEGylated CS and CSA nanoparticles (**Figure S7a, b**), which shows a positive linear relationship with concentration (**Figure S7c, d**). The results show that the extinction coefficient of CSA nanoparticles at 808 nm ( $24.9 \text{ Lg}^{-1}\text{cm}^{-1}$ ) is much higher than that of CS nanoparticles at the same wavelength ( $11.9 \text{ Lg}^{-1}\text{cm}^{-1}$ ). To further distinguish the synergetic effect and additive effect, another two control groups were used for the photothermal conversion experiments: (1) Au nanoparticle solution (the size and concentration of Au nanoparticles are matched to that in the heterogenous CSA nanoparticles); and (2) a mixture of CS and Au nanoparticles in the same ratio as determined in the CSA heterostructures (refer to as CS + Au). The Au nanoparticles were synthesized in an aqueous solution in the presence of BSA under ambient conditions ( $7.4 \pm 0.9 \text{ nm}$ , **Figure S8 a-b**). The obtained spherical Au nanoparticles have the characteristic plasmonic absorbance at around 520 nm (**Figure S8 c**), which is similar to that of gold in CSA nanoparticles.

The concentration of Au nanoparticles is  $22 \mu\text{g mL}^{-1}$ , same to the content of Au in

the CSA heterostructures (the absorbance of CSA nanoparticles at 808 nm is 0.28). The concentration of the mixture of CS and Au nanoparticles is same to that of CSA nanoparticles ( $C = 47 \mu\text{g mL}^{-1}$ ) (**Table S2**). An 808 nm NIR laser ( $0.75 \text{ W cm}^{-2}$ ) was used to heat these two solutions for 9 min. After the laser was turned off, the solutions were naturally cooled to room temperature (**Figure S9**). The photothermal conversion efficiencies of CSA, CS, Au, and mixture of CS + Au nanoparticles were calculated to be 80.8%, 71.7%, 47.1% and 59.0%, respectively (**Figure S10**). Obviously, the formation of heterostructures boosted the photothermal conversion performance of CS nanoparticles due to the synergetic interactions with plasmonic Au nanoparticles. The photothermal stability was also investigated and **Figure 2a** shows the excellent photothermal stability of PEGylated CSA solution over five cycles of heating/cooling processes.

These above results demonstrate the significance of the formation of heterostructures for improving their photothermal conversion efficiency. To further correlate the temperature increment with the concentration of heterostructures over an irradiation time, different concentrations of PEGylated CSA nanoparticles ( $0\text{--}160 \mu\text{g mL}^{-1}$ ) were heated by an 808 nm NIR laser ( $0.75 \text{ W cm}^{-2}$ ) for 10 min. The change of solution temperature was recorded by an infrared thermal imaging camera. **Figure 2b, c** clearly reveals the dependence of the temperature increment on the nanoparticle concentration, *e.g.*, the temperature of  $160 \mu\text{g mL}^{-1}$  solution could rapidly rise from  $30.0^\circ\text{C}$  to  $74.5^\circ\text{C}$  within 10 min. The temperature increment ( $44.5^\circ\text{C}$ ) is much higher than that of pure water ( $2^\circ\text{C}$ ).

The excellence of CSA nanoparticles in photothermal conversion guarantees their performance in PA imaging and PTT. **Figure 2d** clearly shows that the *in vitro* PA imaging signal under 680 nm excitation drastically increased with CSA concentration from 0 to 6.25, 12.5, 25, 50, and 100  $\mu\text{g mL}^{-1}$ . Before the test of their capability of photoablation of tumor cells, their cytotoxicity towards 4T1 tumor cells and 3T3 normal cells was investigated to determine the highest nanoparticle concentration used for the subsequent experiments. The cell viabilities are strongly dependent on the concentration of PEGylated CSA nanoparticles, and more than 80% of the 4T1 cells and 3T3 cells were survived when they were cultured with 80  $\mu\text{g mL}^{-1}$  CSA solution (**Figure 2e**). The cytotoxicity of CSA nanoparticles is slightly higher than that of CS and Au nanoparticles, evidenced by high cell viabilities of 4T1 cells and 3T3 cells (**Figure S8d and Figure S11**) after cultured with the same concentration of CS and Au nanoparticles (80  $\mu\text{g mL}^{-1}$ ). In addition, the cell viability of 3T3 cells cultured with CSA nanoparticles and Au nanoparticles is higher than that of 4T1 cells, demonstrating their higher toxicity to cancer cells than to normal cells.

The cytotoxicity results suggest that the concentration of CS and CSA nanoparticles applied to tumor cells should be lower than 80  $\mu\text{g mL}^{-1}$ . 4T1 cells were respectively cultured with 0, 30, and 60  $\mu\text{g mL}^{-1}$  of CS and CSA nanoparticles for 24 h, and subsequently exposed to 808 nm laser light for 5 min under power density of 0, 0.75, 1, and 1.5  $\text{W cm}^{-2}$ , respectively. After that, a Live/Dead kit was used to test the activity of 4T1 cells, in which the living cells were stained green and dead cells were stained red. **Figure 2f and Figure S12** reveal the effects of the nanoparticle concentration and

the power density of the laser on the ablation of 4T1 cells. The amount of dead cells (red) obviously increased with increasing concentrations of both types of nanoparticles and with the power density of the laser.

After exposed to 808 nm laser light for 5 min under power density of 0, 0.75, 1, and 1.5 W cm<sup>-2</sup>, 4T1 cells were continually cultured for another 24 hours for testing their viabilities. The results in **Figure S13** show that the viabilities of 4T1 cells are similar and above 90% after they were incubated with different concentrations of CS and CSA nanoparticles (30 µg mL<sup>-1</sup> and 60 µg mL<sup>-1</sup>), and then irradiated without or with low power intensity (0.75 W cm<sup>-2</sup>). The temperature variation of cells is around 4 °C after heating for 5 min. When the laser power intensity was increased to 1.0 W cm<sup>-2</sup>, the cell viability decreased with the increase of concentrations of CS and CSA nanoparticles, and only 50% cells survived after incubation with 60 µg mL<sup>-1</sup> CSA nanoparticles and then following irradiation. The temperature variation of cells is between 4 °C and 10 °C after heating for 5 min, depending on the concentration of nanoparticles. Further increasing the laser intensity to 1.5 W cm<sup>-2</sup>, the cell viability drastically decreased, particularly for the cells cultured with high concentration of CSA nanoparticles (60 µg mL<sup>-1</sup>), and the survival rate is less than 5%. The corresponding temperature variation of cells is between 8.5 °C and 16 °C.

The above results demonstrate that CSA nanoparticles exhibited better photothermal conversion performance than CS nanoparticles, and could be used for *in vitro* ablation of cancer cells. The suitable laser power intensity is 1.5 W cm<sup>-2</sup> for ablation. The results further demonstrate the significance of the formation of CSA heterostructures.

As mentioned previously, CSA heterostructures are expected to significantly improve the sensitivity of tumor cells towards X-rays. To reveal the synergetic interactions of copper selenide and gold components in the heterostructure with X-rays, the *in vitro* CT imaging performance of CSA, CS, Au, CS + Au mixture, and commercial iopromide (I) is compared in **Figure 3a**, which shows their dependence of CT values and images on concentrations. When their mass concentrations were varied from 0 to 0.5, 1, 2, and 4 mg mL<sup>-1</sup>, the efficiencies of CSA, CS, Au, CS + Au, and I for attenuation of X-rays were about 84.6, 34.7, 39.5, 34.1 and 37.7 HU Lg<sup>-1</sup>, respectively, which indicate the stronger interactions between CSA nanoparticles and X-rays in comparison with I, CS nanoparticles, Au nanoparticles, and CS + Au mixture. The better *in-vitro* CT performance of heterostructured CSA nanoparticles demonstrates the synergetic effects of multi-components and the significance of growth of heterostructures.

The overall X-ray attenuation coefficients ( $\mu$ ) of CSA and CS nanoparticles can be considered as the sums of the contributions of each element, and can be roughly calculated by the following Eqs. (1, 2):

$$\mu_{CuSe_{2.26}Au_{1.75}} = 0.11\mu_{Cu} + 0.30\mu_{Se} + 0.59\mu_{Au} \tag{1}$$

$$\mu_{Cu_{1.86}Se} = 0.60\mu_{Cu} + 0.40\mu_{Se} \tag{2}$$

where  $\mu_{Cu}$ ,  $\mu_{Se}$ , and  $\mu_{Au}$  are the attenuation coefficients of Cu, Se, and Au. The calculated coefficients are 3.55 m<sup>2</sup>g<sup>-1</sup> for CSA nanoparticles and 1.89 m<sup>2</sup>g<sup>-1</sup> for CS nanoparticles for 60 keV X-rays. Their effective atomic numbers ( $Z$ ) can be estimated by Eqs. (3, 4):

$$\bar{Z} = \sqrt[2.94]{Z_{Cu}^{2.94} + 2.26Z_{Se}^{2.94} + 1.75Z_{Au}^{2.94}} \tag{3} \quad \bar{Z} =$$

$$\sqrt[2.94]{1.86Z_{Cu}^{2.94} + Z_{Se}^{2.94}} \quad (4)$$

where  $Z_{Cu}$ ,  $Z_{Se}$ , and  $Z_{Au}$  are the atomic numbers of Cu, Se, and Au. The calculated  $\bar{Z}$  of CSA and CS nanoparticles are 99.9 and 44.2, respectively. Obviously, both  $\mu$  and  $\bar{Z}$  of CSA heterostructures are much higher than those of CS nanoparticles, which proves that the growth of Au on  $Cu_{2-x}Se$  nanoparticles can enhance their attenuation to X-rays. In addition, the  $\bar{Z}$  of CSA heterostructures is also higher than Au nanoparticles, although their  $\mu$  is slightly smaller than that of Au nanoparticles ( $4.26 \text{ m}^2\text{g}^{-1}$ ).

The above higher X-ray absorption coefficients indicate they could serve as radiosensitizer for radiotherapy. To further examine the radio-enhancement of CS, Au, CS + Au mixture, and CSA nanoparticles, a colony formation assay was conducted. 4T1 cells were cultured with CS, Au, CS + Au mixture, and CSA nanoparticles ( $60 \mu\text{g mL}^{-1}$ ), and subsequently irradiated with 0, 2, 4, 6, and 8 Gy X-rays. The survival rates ( $S$ ) and pictures of cells, as shown in **Figure 3b** and **Figure S14**, exhibit a decreasing trend with increasing dose of X-rays. When 4T1 cells are exposed to the same X-rays, the survival rates of cells treated with nanoparticles are lower than those of the control group without nanoparticles, and follow an order of  $S_{CSA} < S_{Au} < S_{CS} < S_{CS+Au} < S_{ctrl}$ . The surviving cells cultured with CSA nanoparticles are much less than those from other groups. The dependence of  $S$  on the dose of X-rays can be described by Eq. (5):

$$S = 1 - (1 - \exp(-D/D_0))^N \quad (5)$$

$S$  is the survival rate of cells at a given dose,  $D$  is the dose of X-rays,  $D_0$  is the average lethal dose of X-rays, which represents the sensitivity of cells to radiation, and  $N$  is an indicator of cell self-repairing ability.

The values of  $D_0$  for cells from the control group without sensitizer, the CS group, the Au group, the CS + Au group and the CSA group are 1.8, 1.7, 1.5, 1.78 and 1.1 Gy, respectively, which means that CSA nanocrystals taken up by cells significantly improve the sensitivity of the cells to X-rays. In addition, the sensitivity enhancement ratio (SER), a very important parameter to assess the efficiency of radio-enhancement, can be calculated by Eq. (6):

$$SER = D_0(\text{without sensitizer}) / D_0(\text{with sensitizer}). \quad (6)$$

The SER values of CS nanoparticles, Au nanoparticles, CS + Au mixture, and CSA nanoparticles are calculated to be 1.1, 1.2, 1.01, and 1.6, respectively, which demonstrates the radioenhancement of CS nanoparticles has been significantly improved after growth of Au nanoparticles.

It is well known that X-rays mainly damage DNA strands of cells, and  $\gamma$ -H2A.x analysis is commonly used to characterize such damage. **Figure 3c** illustrates the damage to DNA strands of 4T1 cells treated with CS, Au, CS + Au mixture, CSA, X-rays, CS + X-rays, Au + X-rays, CS + Au + X-rays and CSA + X-rays, respectively. The images clearly show the drastic differences from the different treatments, with the most serious DNA damage caused by X-rays in the presence of CSA nanoparticles. These results further illustrate the synergetic effects of heterostructured CSA nanoparticles rather than additive effect.

The apoptosis assay was performed by flow cytometry after 4T1 cells were incubated with CS, Au, CS + Au, CSA nanoparticle solutions and irradiated with 6 Gy of X-rays. As shown in **Figure S15**, X-ray irradiation could improve the apoptosis of cells after



1  
2  
3  
4 cultured with  $60 \mu\text{g mL}^{-1}$  of nanoparticle solutions, particularly for CSA nanoparticles  
5  
6  
7 which can increase the apoptosis of 4T1 cells from 9.82% to 30.28% when 6 Gy X-rays  
8  
9 were applied. The apoptosis of cells cultured with CSA nanoparticles (30.28%) is much  
10  
11 higher than that obtained from the mixture of CS + Au nanoparticles (15.63%) due to  
12  
13 the enhanced sensitization.  
14  
15

16  
17 The above results show that the CSA nanoparticles has an obvious improvement in  
18  
19 photothermal conversion and radio-enhancement, which illustrates their great potential  
20  
21 in PTT and RT. In order to prove whether PTT and RT have synergetic effects on tumor  
22  
23 treatment, the isobologram analysis is employed. As shown in **Figure 3D** and **Table**  
24  
25 **S3**, the inhibitory effect of PTT and RT on 4T1 cells is synergistic, evidenced by the  
26  
27 fact that data points in the isobologram are below the line of additive effect. In addition,  
28  
29 **Figure S16** and **Table S4** demonstrate the synergistic interactions on enhanced  
30  
31 anticancer efficacy between Au NPs and CS NPs.  
32  
33  
34  
35  
36  
37

38 The above synergetic interactions in CSA heterostructures suggest their advantages  
39  
40 in multimodal imaging and combined radiophotothermal therapy. Before the  
41  
42 PEGylated CSA nanoparticles are intravenously injected for these applications, it is  
43  
44 important to know their blood circulation time, which is essential for both imaging and  
45  
46 therapy of tumors. Therefore, the PEGylated CSA nanoparticles were injected into the  
47  
48 four healthy BALB/c mice through their tail veins. Their blood was collected at  
49  
50 different times after injection and digested with chloroazotic acid ( $\text{HCl}:\text{HNO}_3 = 3:1$  by  
51  
52 volume), and then the copper contents were quantified by ICP-OES. The blood  
53  
54 circulation time was determined by fitting the time-dependent decay of the copper  
55  
56  
57  
58  
59  
60

contents with a two-compartmental model. As shown in **Figure S17**, CSA nanoparticles have a blood circulation time of about 3.4 h, which ensures their circulation and accumulation in tumor for imaging and therapy.

For an exogenous material such as CSA nanoparticles, an important issue is their immunological response after intravenous injection.<sup>53, 54</sup> As blood contains a number of immunological and metabolic indicators, blood analyses are usually preformed to assess immunological responses and metabolism of CSA nanoparticles. Five groups of healthy mice were administrated with PEGylated CSA solution through their tail veins (the dose: 25 mg kg<sup>-1</sup>). Their blood was collected for analyses at different time intervals, and there was no difference in the red blood cells (RBC), hemoglobin (HGB), mean corpuscular volume (MCV), and hematocrit (HCT) (**Figure 4a, b, c, d**, respectively) for the blood collected before and after administration of CSA nanoparticles. White blood cells (WBC) (**Figure 4e**) gradually decreased in the first week after injection of CSA nanoparticles, which illustrates that the body produced a certain stress inflammatory response after administration of CSA nanoparticles. The level of platelets (PLT) (**Figure 4f**) also decreased in the first three days and then gradually increased to the normal level, which suggests that the body suffered from slight stress hypersplenism. After 14 days of the injection, both WBC and PLT had recovered to around the normal level, indicating that the stress inflammatory response is not serious, and that it was possible to recover to the normal situation by the self-repair of the body. Alanine aminotransferase (ALT) and aspartate aminotransferase (AST) are major indexes of liver function, which are sensitive to damage to liver cells. Urea nitrogen (UREA) is

the hallmark of renal function, which could reflect the renal damage situation. As shown in **Figure 4g, h**, ALT turned out to have a higher level than normal on first day after injection, and then it began to constantly decrease and recovered to normal at 14 days post injection. AST was slightly higher than the normal level in the first week post injection, and it also recovered to the normal level after 14 days. This illustrates that, although the accumulation of CSA in liver could induce a slight stress on the liver cells, they could recover after a few days. In addition, the level of UREA (**Figure 4i**) was almost the same as that of the control group, which suggests that the metabolism of CSA nanoparticles has no side effects on renal function. The above results demonstrate that low dose of heterogeneous PEGylated CSA nanocrystals ( $25 \text{ mg kg}^{-1}$ ) couldn't induce irreversible damage to health. Their immune response could be minimized by further surface modification.

To examine their performance in imaging of orthotopic tumor, BALB/c female mice bearing 4T1 tumors at the second pair of breasts were administrated with PEGylated CSA nanoparticles ( $200 \text{ }\mu\text{L}$ ,  $2.5 \text{ mg mL}^{-1}$ ) through tail veins, and PA images of the tumor were collected to indicate the accumulation of nanoparticles within tumor. **Figure 5a** clearly shows a very weak PA signal in the tumor region before injection of PEGylated CSA solution, and gradual enhancement to the maximum around 10 h post injection. The maximal PA signal is nearly 3 times higher than that acquired before the injection of the PEGylated CSA nanoparticles (**Figure S18a**). The results indicate the dynamic accumulation and clearance of CSA nanoparticles within tumor, and the best treatment time is around 10 h post injection of nanoparticles.

As PA imaging has difficulty in quantifying nanoparticles accumulated within tumor, highly sensitive SPECT/CT imaging was used. The PEGylated CSA nanoparticles were efficiently labeled with the radioisotope  $^{99m}\text{Tc}$  to achieve a radiolabeling yield of 92%, which ensures their excellent performance in SPECT/CT imaging. **Figure 5b** shows typical SPECT/CT images of a tumor-bearing mouse acquired after administration of  $^{99m}\text{Tc}$ -CSA nanoparticles. The tumor area marked by the white circle presents an obvious gradual enhancement in signal, and the maximum was achieved at 8 h post injection. After the end of the experiment, the major organs and tumor were harvested from the mice for quantification of accumulated nanoparticles by counting  $\gamma$ -rays (**Figure S18 b**). The results show that the accumulation of CSA nanoparticles in the tumor was 1.2% ID  $\text{g}^{-1}$  (injection dose per gram) after 24 h post injection, and most CSA nanoparticles were accumulated in the liver and spleen due to their rich phagocytes.

Both PA imaging and SPECT/CT imaging clearly show the accumulation of CSA nanoparticles at tumor site, however, which were not sufficient for CT imaging. To demonstrate their potential in *in vivo* CT imaging, a female mouse was inoculated with two 4T1 tumors on the left and right breasts of the second pair, respectively. Then, the same doses ( $30 \text{ mg kg}^{-1}$ ) of CSA and I solutions were intra-tumorally injected into the left and right tumors, respectively. Compared with CT images obtained before and after injection, the left tumor is much brighter than the right one in the CT image after the injection of CSA and I solutions (**Figure 5c-d**), and their CT values were 809.4 and 103.1 HU, respectively. The three dimensional (3D) CT images also clearly show the

enhancement after injection of CSA nanoparticles (**Figure S19**). The results demonstrate the better performance of CSA nanoparticles than commercial iopromide in CT imaging when sufficient CSA nanoparticles are accumulated within the tumor. The above imaging results demonstrate the promise of heterostructured CSA nanoparticles in multimodal imaging, which could combine their different advantages to overcome the limitations of individual imaging and provide complementary information for accurate diagnosis.

In addition to multimodal imaging, the previous *in vitro* results also demonstrate the potential of CSA heterostructures serving as sensitizer for radiophotothermal therapy of tumors. To demonstrate their feasibility, seven groups of 4T1-tumor bearing mice respectively received different treatments, *i.e.*, i) injection of PBS solution (control group), ii) injection of CSA nanoparticle solution (CSA group), iii) irradiation with X-rays (RT group), iv) irradiation with an 808 nm NIR laser (PTT group), v) injection of CSA nanoparticle solution and then irradiation with X-rays (CSA + RT), vi) injection of CSA nanoparticle solution and irradiation with an 808 nm NIR laser (CSA + PTT), and vii) injection of CSA nanoparticles and then irradiation with X-rays and an 808 nm NIR laser (CSA + PTT + RT group). Compared with mice injected with PBS solution, the tumor temperature of mice injected with PEGylated CSA nanoparticles could rapidly rise to 60 °C within 10 min after irradiation with an 808 nm laser ( $1.5 \text{ W cm}^{-2}$ ) (**Figure 6a-b**). The weights of mice and the sizes of the tumors were constantly measured and recorded every two days. **Figure S20** displays photographs of the mice that received different treatments after different numbers of days, which shows that

only the tumors from the mice in the CSA + PTT and CSA + PTT + RT groups were ablated because of the excellent photothermal conversion and the synergy of radiophotothermal therapy. The weights of mice from the control group and the other treated groups were similar, and slightly fluctuated with the culture time (**Figure 6c**). The variation in tumor volume in **Figure 6d** shows that the mice only injected with CSA nanoparticles experienced the same trend as the control group. The relative tumor volume of the mice treated with radiotherapy or photothermal therapy alone was slightly smaller than that in the control group, which illustrates that RT and PTT could mildly inhibit the growth of the tumors. Moreover, the antitumor efficacy of photothermal therapy was better than that of radiotherapy. When the mice were injected with CSA and irradiated with X-rays, their relative tumor volume became smaller than that of the mice only irradiated with X-rays, proving the enhancement effect of CSA nanoparticles on radiotherapy. The tumors of mice treated with radiophotothermal therapy after injection of CSA nanoparticles were successfully ablated without relapse.

The relative survival rates can also reflect the difference in efficacy of various treatments (**Figure 6e**). The relative survival rate of mice in the combined therapy group was 100% (n = 5), which proves the superior synergetic effects of radiotherapy and photothermal therapy. The relative survival rate of mice in the CSA + PTT group was 80%, which is higher than that in the CSA + RT group (40%). When compared with the 100% survival rate of mice in the CSA + PTT + RT group, it becomes clear that both PTT and RT have a certain antitumor effect. Only 20% of the mice from the PTT treatment group survived, and none survived in the other three groups, which

further verifies the excellence of CSA nanoparticles in synergetic radiophotothermal therapy.

In order to further confirm the treatment efficacy, the major organs of mice from each group were harvested and cut into slices for histochemical analysis through staining with hematoxylin and eosin (H&E). Noticeable lung metastasis can be found on the surface of lungs and their slices stained with H&E in the groups of mice treated with PBS, CSA, RT, PTT, CSA + RT, and some lungs had lost their normal structure (**Figure 6f**). Moreover, serious liver metastasis (**Figure S21**) from the original subcutaneously inoculated tumor can also be found in the mice from several groups, except for the CSA + RT + PTT group. It should be noted that although 80% mice in the group of CSA + PTT were survived, there were some tumor metastases to lung and liver in the 20% of dead mice in this group (**Figure S22**). The results demonstrate the necessity of combined radiophotothermal therapy for successful treatment of a tumor without metastasis by using CSA nano-heterostructures.

## CONCLUSIONS

In summary, PEGylated copper selenide-gold hetero-nanocrystals were successfully prepared by taking advantage of spontaneous redox reactions between copper selenide nanoparticles and  $\text{HAuCl}_4$  solution at room temperature. The resultant hetero-nanostructures possess better performance in terms of photothermal conversion ( $\eta = 80.8\%$ ) and attenuation of X-rays ( $86.1 \text{ HU Lg}^{-1}$ ), than the individual fragments and their mixture due to the strong synergetic effects. These properties ensure their

performance in simultaneously serving as a promising photothermal transducer and radiosensitizer for multimodal imaging guided radiophotothermal treatment of orthotopic breast cancer. Our work demonstrates that the hetero-nanostructures engineered from high- and low Z elements could be a generation of theranostic agents with enhanced radiosensitizing and photothermal performance through the synergetic effects.

## MATERIALS AND METHODS

**Materials.** Copper sulfate ( $\text{CuSO}_4 \cdot 5\text{H}_2\text{O}$ ), bovine serum albumin (BSA), and chloroauric acid tetrahydrate ( $\text{HAuCl}_4 \cdot 4\text{H}_2\text{O}$ ) were bought from Sinopharm Chemical Reagent Co. Ltd. Selenium dioxide ( $\text{SeO}_2$ ) was purchased from Aladdin Chemistry Co. Ltd. Vitamin C was obtained from Alfa Aesar Co. Ltd. Dimercapto-poly(ethylene glycol) (HS-PEG-SH, MW = 5000) was purchased from Adamas Co. Ltd. All chemicals were used as received without further purification.

**Synthesis of  $\text{Cu}_{2-x}\text{Se}$  Nanocrystals and PEGylated  $\text{Cu}_{2-x}\text{Se-Au}$  Hetero-nanocrystals.**  $\text{Cu}_{2-x}\text{Se}$  nanoparticles were synthesized based on previous work with a slight modification.<sup>52</sup> 55 mL Milli-Q water ( $> 18 \text{ M}\Omega \cdot \text{cm}$ ) and 16 mL BSA solution ( $10 \text{ mg mL}^{-1}$ ) were added into a round-bottomed flask, followed by addition of 1 mL  $\text{SeO}_2$  solution (0.2 M) and 3 mL Vitamin C solution (0.4 M). The mixture was stirred for 15 min and turned red due to the reduction of  $\text{SeO}_2$ , which means the formation of Se nanoparticles. Meanwhile, freshly prepared  $\text{CuSO}_4 \cdot 5\text{H}_2\text{O}$  (1 mL, 0.4 M) solution was rapidly mixed with Vitamin C solution (4 mL, 0.4 M) under vigorous stirring. The



resultant green mixture was quickly poured into the Se solution to generate a dark brown solution, which gradually turned deep green after reaction for 30 h at room temperature, due to the formation of  $\text{Cu}_{2-x}\text{Se}$  nanoparticles (NPs). The resultant nanoparticles were centrifuged twice at 20000 rpm and washed with Milli-Q water to get rid of extra BSA and Vitamin C.

The purified  $\text{Cu}_{2-x}\text{Se}$  NPs were re-dissolved in 30 mL water, and then the  $\text{HAuCl}_4$  solution was added into it with a molar ratio of  $\text{Cu}_{2-x}\text{Se} : \text{HAuCl}_4 = 1 : 0.75$ . After the mixture was reacted for 3 h, the final products were centrifuged at 20000 rpm and re-dispersed in Milli-Q water. Then, 0.05 g HS-PEG-SH was poured into the solution and stirred for 6 h. The PEGylated  $\text{Cu}_{2-x}\text{Se-Au}$  nanoparticles were purified by the similar method, and then stored in fridge (4 °C) for later characterization and experiments.

**Synthesis of Au Nanocrystals.**  $\text{HAuCl}_4$  solution (800  $\mu\text{L}$ , 1 wt%) was mixed with BSA solution (50 mL, 0.1  $\text{mg mL}^{-1}$ ) in a round-bottomed flask. The mixture was stirred for 1 min and then 90  $\mu\text{L}$  freshly prepared  $\text{NaBH}_4$  solution was rapidly added under vigorous stirring. The solution was quickly turn to claret-red solution. After reaction for 1 h at room temperature, 0.03 g PEG-SH was added to modify the resultant Au nanoparticles. The modified Au nanoparticles were separated by centrifugation at 20000 rpm and washed with Milli-Q water to remove the impurities.

**Characterization.** The UV-Vis-NIR absorbance was recorded on a PerkinElmer Lambda 750 spectrophotometer. The morphology of nanoparticles was observed under a FEI Tecnai G20 transmission electron microscope operating at 200 kV. The high-resolution TEM images and STEM-EDS spectra were captured with a JEOL ARM-

200F operating with an EDAX solid-state X-ray detector at 200 kV. The crystal structure of nanoparticles was determined by a Shimadzu XRD-6000 X-ray powder diffractometer equipped with Cu K $\alpha_1$  radiation ( $\lambda = 0.15406$  nm). X-ray photoelectron spectroscopy (XPS) was used to characterize the valence states of elements, and was conducted with a Thermo Scientific Sigma Probe instrument, which uses Al K $\alpha$  X-ray radiation and fixed analyzer transmission mode.

To examine the photothermal performance of heterogeneous CSA nanocrystals, different concentrations (0, 7.3, 14.5, 29, 58, and 116  $\mu\text{g mL}^{-1}$ ) of CSA solutions were prepared and heated with an 808 nm laser ( $0.75 \text{ W cm}^{-2}$ , 10 min). An infrared thermal imaging camera (FLIR, A65) was applied to record the change of temperature. The photothermal stability of CSA nanoparticles was also examined by heating and cooling for 5 cycles. For each cycle, 808 nm laser ( $0.75 \text{ W cm}^{-2}$ ) was turned on to heat the CSA solution for 10 min and then switched off to allow naturally cooling to room temperature.

To calculate its photothermal conversion efficiency ( $\eta$ ), a diluted CSA solution was irradiated by an 808 nm laser ( $0.75 \text{ W cm}^{-2}$ , 9 min). The solution was cooled after switching off the laser. Meanwhile, the CS solution was also prepared and similarly irradiated with the laser to compare their  $\eta$ , which was obtained according to the Eqs. (7, 8, 9):

$$\eta = \frac{m * c * (T_{max} - T_{surr})}{I * (1 - 10^{-A}) * \tau_s} \quad (7)$$

$$\tau_s = \frac{-t}{\ln \theta} \quad (8)$$

$$\theta = \frac{T - T_{surr}}{T_{max} - T_{surr}} \quad (9)$$

Where  $m$  is the mass of nanoparticle solution, which is 1 g here,  $c$  is the specific heat capacity of water ( $4.2 \text{ J g}^{-1}$ ),  $T_{max}$  is the highest temperature of the solution sample and  $T_{surr}$  is the room temperature ( $\Delta T = T_{max} - T_{surr}$ ). The calculated  $\Delta T$  values of the CSA and CS solutions were  $28.3^\circ\text{C}$  and  $23.6^\circ\text{C}$ , respectively.  $A$  is the absorbance of the sample at 808 nm, which is 0.28 for both CSA solution and CS solution.  $\tau_s$  is the system time constant of the sample (413.7 s for CSA and 390.0 s for CS).  $t$  is the cooling time.  $T$  is the temperature of the solution during the cooling process. According to the above equations, the photothermal conversion efficiencies of the CSA and CS nanoparticles were calculated to be 80.8% and 71.7%, respectively.

To distinguish the synergetic effect and additive effect in the CSA heterostructures, 7 nm Au nanoparticle solution and a mixture of CS and Au nanoparticles in the same ratio as in the CSA heterostructures (refer to as CS + Au) were used as control for the photothermal conversion experiments. The concentrations of Au nanoparticles and the mixture of CS and Au nanoparticles are  $22 \mu\text{g mL}^{-1}$  and  $47 \mu\text{g mL}^{-1}$ , respectively. An 808 nm NIR laser ( $0.75 \text{ W cm}^{-2}$ ) was used to heat these two solutions for 9 min, and then turned off to allow the solutions naturally cooling to room temperature. The photothermal conversion efficiencies ( $\eta$ ) of Au nanoparticles and CS + Au mixture were calculated to be 47.1 % and 59.0 %.

**Cytotoxicity Assays.** The cytotoxicity of the PEGylated CSA and PEGylated CS nanocrystals was assessed by the standard 3-(4,5dimethylthiazol-2-yl)-2,5-diphenyltetrazolium bromide (MTT) assay. 4T1 cells were planted into 96 well plates (~8000 cells per well) and incubated in Roswell Park Memorial Institute (RPMI) (1640)

medium at 37 °C in a 5% CO<sub>2</sub> atmosphere for 24 h. Then different concentrations (0, 5, 10, 20, 40, 80, 160 µg mL<sup>-1</sup>) of CSA, CS and Au nanoparticles were added after removal of the RPMI (1640) medium, and the cells were cultured for another day. After that, MTT solution (100 µL, 0.5 mg mL<sup>-1</sup>) was added into each well, and the cells were cultured with MTT at 37 °C for 24 h. After removal of the MTT solution, dimethyl sulfoxide (DMSO, 100 µL) was used to dissolve the formed formazan crystals. The relative viability of 4T1 cells was expressed by the relative absorbance at 570 nm.

To investigate the difference of toxicity of nanoparticles to tumor cells and normal cells, 3T3 cells were also selected for incubation with CSA, CS, and Au nanoparticles under the same conditions. The similar MTT assay was used to test the cell viability.

**Photothermal Ablation of Cancer Cells.** 4T1 cells were seeded in 12 well plates (2 × 10<sup>5</sup> cells per well) and cultured with PEGylated CSA and CS at concentrations of 0, 30, and 60 µg mL<sup>-1</sup>. Then, all the cells were irradiated with an 808 nm laser for 5 min, under power density of 0, 0.75, 1, and 1.5 W cm<sup>-2</sup>, respectively. Then, a live/dead kit was used to stain the live cells (green) and the dead cells (red), which can be distinguished with a fluorescence microscope (Leica).

To quantify the survival rates and temperature variation of 4T1 cells, they were seeded in 96 well plates (8000 cells per well) and cultured with PEGylated CSA and CS nanoparticles at concentrations of 0, 30, and 60 µg mL<sup>-1</sup>. Then, all the cells were irradiated with an 808 nm laser for 5 min under power density of 0, 0.75, 1, and 1.5 W cm<sup>-2</sup>, respectively. An infrared imaging camera was used to monitor temperature variation of cells. After irradiation, the cell viability was assessed by the standard MTT

assay.

**Colony Formation.** 4T1 cells were cultured with the same concentrations of CS nanoparticles, Au nanoparticles, CS + Au mixture, and CSA nanoparticles ( $60 \mu\text{g mL}^{-1}$ ) for 12 h, and subsequently irradiated with 0, 2, 4, 6, and 8 Gy X-rays. After incubation for 12 days, the number of colonies, indicated by the staining of crystal violet, was counted.

**DNA Damage Detection.** 4T1 cells were cultured with PEGylated CS, Au, CS + Au, and CSA nanoparticles ( $60 \mu\text{g mL}^{-1}$ ) for 12 h, and then exposed to 6 Gy X-rays. The supernatant was removed after 1.5 h, and the 4T1 cells were immersed in 4% paraformaldehyde fixation for 15 min and then washed with PBS three times. After that, the cells were treated with Triton X-100 for 30 min to damage their membranes. Then, the cells were soaked in a blocking buffer (1% bovine serum albumin in tris-buffered saline solution) for 1 h, and incubated with anti-histone  $\gamma\text{H2A.x}$  mouse monoclonal antibodies (diluted 1:500 with PBS) in the dark overnight at 4 °C, followed by washing with PBS three times. The cells were further cultured with sheep anti-mouse secondary antibody (diluted 1:2000 with PBS) for 2 h in the dark and then washed with PBS three times. Finally, 10  $\mu\text{L}$  Hoechst was used to stain the cells for 15 min, and the stained cells were observed with the confocal microscope (PerkinElmer UltraViewVoX).

**Apoptosis Assay.** 4T1 cells were planted in 6-well plates with a concentration of  $3 \times 10^5$  cells/well and cultured under the conditions of 37 °C and 5%  $\text{CO}_2$  for 24 h. They were then incubated with CS, Au, CS + Au, CSA nanoparticle solutions ( $60 \mu\text{g mL}^{-1}$ ) for 12 h, respectively, and irradiated with X-rays at a dose of 6 Gy. After incubation for

another 36 h, the cells were collected and stained with Annexin V/PI, and then analyzed with flow cytometry.

**Isobologram Analysis.** A curve was plotted with the IC<sub>50</sub> values of laser and X-ray as the X- and Y-axes, respectively. The point in the isobologram represents the power density of laser and dose of X-rays at the IC<sub>50</sub> value of the combined treatment. If the data point falls on the straight line, the interaction between laser and X-rays is an additive effect. If the point lies above or below the straight line, it represents antagonism or synergism effect, respectively.<sup>55</sup>

**Blood Circulation Time.** The blood circulation behavior of CSA nanoparticles in healthy BALB/c mice were investigated by intravenous administration of PEGylated nanoparticles. The blood was withdrawn from the mice at post injection 15 min, 30 min, 1 h, 2 h, 4 h, 6 h, 8 h, 12 h, 24 h, 48 h, and 72 h, and copper contents in the blood were measured by ICP-OES after it was digested with chloroazotic acid (HCl: HNO<sub>3</sub> = 3:1 in volume).

**Blood Routine and Biochemistry Assay.** The blood routine and biochemistry assay were performed with four groups of healthy mice (n = 4). Their blood was collected at day 1, day 3, day 7, and day 14 after they were administrated with PEGylated CSA solution through their tail veins. The blood was also withdrawn from another four mice without injection of CSA nanoparticles as a reference. Red blood cells (RBC), white blood cells (WBC), platelets (PLT), and blood indices, including hemoglobin (HGB), mean corpuscular volume (MCV), hematocrit (HCT), total protein (TP), alanine aminotransferase (ALT), aspartate aminotransferase (AST), and urea nitrogen (UREA),

1  
2  
3  
4 were examined to evaluate the immunity and metabolism situation.  
5

6  
7 **Animal Model.** Mice bearing 4T1 tumors were exografted through subcutaneous  
8  
9 inoculation of  $4 \times 10^6$  cells in 50  $\mu$ L PBS at the second pair of breasts. When the tumor  
10  
11 grew to  $\sim 100 \text{ mm}^3$ , the mice (BALB/c male mice, 5 weeks old) were used for CT  
12  
13 imaging, SPECT/CT imaging, photothermal therapy, radiotherapy, and combined  
14  
15 radiophotothermal therapy. The nude mice exografted with 4T1 tumors were used for  
16  
17 PA imaging. All animal experiments followed the protocols authorized by the Soochow  
18  
19 University Laboratory Animal Center.  
20  
21  
22  
23

24  
25 **Photoacoustic (PA) Imaging.** The performance of CSA nanoparticles in PA  
26  
27 imaging was evaluated with a multispectral optoacoustic tomography scanner (MSOT,  
28  
29 iThera Medical). The *in vitro* imaging was performed with different concentrations of  
30  
31 CSA nanoparticle solutions (0, 6.25, 12.5, 25, 50, and 100  $\mu\text{g mL}^{-1}$ ). The *in vivo*  
32  
33 imaging was carried out with a nude mouse bearing a 4T1 tumor. The pre-contrast  
34  
35 image of tumor was collected before the injection of PEGylated CSA nanoparticle  
36  
37 solution. The mouse was then intravenously injected with CSA nanoparticles and  
38  
39 scanned at 2 h, 4 h, 6 h, 8 h, 10 h, 12 h, and 24 h post injection to show the dynamic  
40  
41 accumulation of nanoparticles at the tumor site.  
42  
43  
44  
45  
46  
47

48  
49 **CT Imaging.** The performance of PEGylated CSA nanoparticles in CT imaging was  
50  
51 compared with PEGylated CS nanoparticles, Au nanoparticles, mixture of CS and Au  
52  
53 nanoparticles, and commercial iopromide *in vitro*. Their mass concentrations were  
54  
55 changed from 0 to 0.5, 1, 2, and 4  $\text{mg mL}^{-1}$ . The *in vivo* CT imaging was conducted  
56  
57 with a BALB/c mouse bearing two similar sized tumors, which were intra-tumorally  
58  
59  
60

1  
2  
3  
4 injected with same doses of CSA nanoparticles and I solutions. The CT images were  
5  
6 collected before and after injection of contrast agent. All the CT images were recorded  
7  
8 on an imaging system (MILabs, Utrecht, the Netherlands), which was operated with  
9  
10 615 mA tube current and 55 kV tube voltage.  
11  
12

13  
14 **SPECT-CT Imaging.** 2 mCi <sup>99m</sup>Tc radionuclides (provided by Shanghai GMS  
15  
16 Pharmaceutical Co., Ltd.) were used to label the PEGylated CSA nanoparticles for  
17  
18 SPECT imaging. 200 μL (2.5 mg mL<sup>-1</sup>) PEGylated CSA nanoparticle solution was  
19  
20 added into a freshly prepared stannous chloride (SnCl<sub>2</sub>, 1 mg mL<sup>-1</sup> in 0.1 M HCl)  
21  
22 solution containing 2 mCi <sup>99m</sup>Tc radionuclides, and reacted for 30 min under ambient  
23  
24 conditions. The mixed solution was ultra-filtrated to remove free <sup>99m</sup>Tc radionuclides,  
25  
26 and the purified <sup>99m</sup>Tc labeled CSA nanoparticle solution was injected into an  
27  
28 anaesthetized BALB/c mouse bearing 4T1 tumor for SPECT/CT imaging, which was  
29  
30 recorded with the MILabs imaging system.  
31  
32  
33  
34  
35  
36

37  
38 **PTT/RT Therapy with CSA Nanoparticles.** To evaluate the anti-tumor efficacy of  
39  
40 CSA nanoparticles, seven groups of 4T1 tumor-bearing BALB/c mice were  
41  
42 respectively treated under different conditions: i) injected with 200 μL PBS (control  
43  
44 group), ii) injected with CSA nanoparticles (CSA group), iii) irradiated with X-rays  
45  
46 (RT group), iv) irradiated with an 808 nm NIR laser (PTT group), v) injected with CSA  
47  
48 nanoparticles and then irradiated with X-rays (CSA + RT group), vi) injected with CSA  
49  
50 nanoparticles and irradiated with the 808 nm NIR laser (CSA + PTT group), and vii)  
51  
52 injected with CSA nanoparticles and then irradiated with X-rays and the 808 nm NIR  
53  
54 laser (CSA + PTT + RT group). The concentration and volume of injected CSA  
55  
56  
57  
58  
59  
60



nanoparticles were  $2.5 \text{ mg mL}^{-1}$  and  $200 \text{ }\mu\text{L}$ , respectively. The power density and the irradiation time used for PTT were  $1.5 \text{ W cm}^{-2}$  and 10 min, respectively. 6 Gy X-rays released with a rate of  $1.01 \text{ Gy min}^{-1}$  were used for RT (Rad Source RS-2000 Pro). During the treatment period, photographs of tumor-bearing mice were collected. The weights and tumor volumes of the mice were also constantly measured and recorded every two days.<sup>11</sup> The survival of mice was recorded for 40 days after the treatment.

**Histology Analysis.** The major organs (*i.e.*, heart, liver, spleen, lung, and kidney) of mice from different groups were harvested and immersed in formalin. Then, the organs were cut into slices and stained with hematoxylin and eosin (H&E). Their structure and cell morphology were recorded with a Leica microscope (DM750).

## ASSOCIATED CONTENT

### Supporting Information

Supporting Information is free and available from the ACS Publications website or from the author, including additional characterization results (particle size distribution, HAADF-STEM images, EDS spectra, XPS, Zeta potential, hydrodynamic size, colloidal stability, UV-VIS absorption, photothermal conversion efficiency) of CS and CSA nanoparticles, cytotoxicity and colony assay of CS and Au nanoparticles, PA signal intensities acquired at different time, CT images, photographs of mice, slices of major organs stained with H&E.

## AUTHOR INFORMATION

### Corresponding Author

\*E-mail: zhenli@suda.edu.cn.

### ORCID

1  
2  
3  
4  
5  
6  
7  
8  
9  
10  
11  
12  
13  
14  
15  
16  
17  
18  
19  
20  
21  
22  
23  
24  
25  
26  
27  
28  
29  
30  
31  
32  
33  
34  
35  
36  
37  
38  
39  
40  
41  
42  
43  
44  
45  
46  
47  
48  
49  
50  
51  
52  
53  
54  
55  
56  
57  
58  
59  
60

Zhen Li: 0000-0003-0333-7699

Mingyuan Gao: 0000-0002-7360-3684

**Notes**

The authors declare no competing financial interest.

**ACKNOWLEDGEMENTS**

Z. Li acknowledges support from the National Key Research and Development Program of China (2018YFA0208800), National Natural Science Foundation of China (81471657, 81527901), the 1000 Plan for Young Talents, and Jiangsu Specially Appointed Professorship. The authors also are grateful for support from the Jiangsu Provincial Key Laboratory of Radiation Medicine and Protection, the Priority Academic Development Program of Jiangsu Higher Education Institutions (PAPD). The authors would like to thank Dr. Tania Silver for helpful discussion of the manuscript.

Received: ((will be filled in by the editorial staff))

Revised: ((will be filled in by the editorial staff))

Published online: ((will be filled in by the editorial staff))

## REFERENCES

- (1) Delaney, G.; Jacob, S.; Featherstone, C.; Barton, M. The Role of Radiotherapy in Cancer Treatment - Estimating Optimal Utilization from a Review of Evidence-Based Clinical Guidelines. *Cancer* **2005**, *104*, 1129-1137.
- (2) Lord, C. J.; Ashworth, A. The DNA Damage Response and Cancer Therapy. *Nature* **2012**, *481*, 287-294.
- (3) Jiang, W.; Li, Q.; Xiao, L.; Dou, J. X.; Liu, Y.; Yu, W. H.; Ma, Y. C.; Li, X. Q.; You, Y. Z.; Tong, Z. T.; Liu, H.; Liang, H.; Lu, L. G.; Xu, X. D.; Yao, Y. D.; Zhang, G. Q.; Wang, Y. C.; Wang, J. Hierarchical Multiplexing Nanodroplets for Imaging-Guided Cancer Radiotherapy via DNA Damage Enhancement and Concomitant DNA Repair Prevention. *ACS Nano* **2018**, *12*, 5684-5698.
- (4) Falk, S. Principles of Cancer Treatment by Radiotherapy. *Surgery (Oxford)* **2006**, *24*, 62-65.
- (5) Schaue, D.; McBride, W. H. Opportunities and Challenges of Radiotherapy for Treating Cancer. *Nat. Rev. Clin. Oncol.* **2015**, *12*, 527-540.
- (6) Begg, A. C.; Stewart, F. A.; Vens, C. Strategies to Improve Radiotherapy with Targeted Drugs. *Nat. Rev. Cancer* **2011**, *11*, 239-253.
- (7) Song, G. S.; Cheng, L.; Chao, Y.; Yang, K.; Liu, Z. Emerging Nanotechnology and Advanced Materials for Cancer Radiation Therapy. *Adv. Mater.* **2017**, *29*, 1700996.
- (8) Zheng, Y.; Hunting, D. J.; Ayotte, P.; Sanche, L. Radiosensitization of DNA by Gold Nanoparticles Irradiated with High-Energy Electrons. *Radiat. Res.* **2008**, *169*, 19-27.
- (9) Goswami, N.; Luo, Z.; Yuan, X.; Leong, D. T.; Xie, J. Engineering Gold-Based Radiosensitizers for Cancer Radiotherapy. *Mater. Horiz.* **2017**, *4*, 817-831.
- (10) Guo, Z.; Zhu, S.; Yong, Y.; Zhang, X.; Dong, X.; Du, J.; Xie, J.; Wang, Q.; Gu, Z.; Zhao, Y. Synthesis of BSA-Coated BiOI@Bi<sub>2</sub>S<sub>3</sub> Semiconductor Heterojunction Nanoparticles and Their Applications for Radio/Photodynamic/Photothermal Synergistic Therapy of Tumor. *Adv. Mater.* **2017**, *29*, 1704136.
- (11) Mao, F. X.; Wen, L.; Sun, C. X.; Zhang, S. H.; Wang, G. L.; Zeng, J. F.; Wang,

- Y.; Ma, J. M.; Gao, M. Y.; Li, Z. Ultrasmall Biocompatible Bi<sub>2</sub>Se<sub>3</sub> Nanodots for Multimodal Imaging-Guided Synergistic Radiophotothermal Therapy against Cancer. *ACS Nano* **2016**, *10*, 11145-11155.
- (12) Wang, Y.; Wu, Y. Y.; Liu, Y. J.; Shen, J.; Lv, L.; Li, L. B.; Yang, L. C.; Zeng, J. F.; Wang, Y. Y.; Zhang, L. S.; Li, Z.; Gao, M. Y.; Chai, Z. F. BSA-Mediated Synthesis of Bismuth Sulfide Nanotheranostic Agents for Tumor Multimodal Imaging and Thermoradiotherapy. *Adv. Funct. Mater.* **2016**, *26*, 5335-5344.
- (13) Wen, L.; Chen, L.; Zheng, S. M.; Zeng, J. F.; Duan, G. X.; Wang, Y.; Wang, G. L.; Chai, Z. F.; Li, Z.; Gao, M. Y. Ultrasmall Biocompatible WO<sub>3-x</sub> Nanodots for Multimodality Imaging and Combined Therapy of Cancers. *Adv. Mater.* **2016**, *28*, 5072-5079.
- (14) Huo, D.; Liu, S.; Zhang, C.; He, J.; Zhou, Z.; Zhang, H.; Hu, Y. Hypoxia-Targeting, Tumor Microenvironment Responsive Nanocluster Bomb for Radical-Enhanced Radiotherapy. *ACS Nano* **2017**, *11*, 10159-10174.
- (15) Yamada, M.; Foote, M.; Prow, T. W. Therapeutic Gold, Silver, and Platinum Nanoparticles. *Wiley Interdiscip. Rev.: Nanomed. Nanobiotechnol.* **2014**, *7*, 428-445.
- (16) Mi, P.; Dewi, N.; Yanagie, H.; Kokuryo, D.; Suzuki, M.; Sakurai, Y.; Li, Y.; Aoki, I.; Ono, K.; Takahashi, H.; Cabral, H.; Nishiyama, N.; Kataoka, K. Hybrid Calcium Phosphate-Polymeric Micelles Incorporating Gadolinium Chelates for Imaging-Guided Gadolinium Neutron Capture Tumor Therapy. *ACS Nano* **2015**, *9*, 5913-5921.
- (17) Fang, J.; Nakamura, H.; Maeda, H. The EPR Effect: Unique Features of Tumor Blood Vessels for Drug Delivery, Factors Involved, and Limitations and Augmentation of the Effect. *Adv. Drug Delivery Rev.* **2011**, *63*, 136-151.
- (18) Li, Z.; Sun, Q.; Zhu, Y.; Tan, B.; Xu, Z. P.; Dou, S. X. Ultra-Small Fluorescent Inorganic Nanoparticles for Bioimaging. *J. Mater. Chem. B.* **2014**, *2*, 2793-2818.
- (19) Jiang, Y.; Cui, D.; Fang, Y.; Zhen, X.; Upputuri, P. K.; Pramanik, M.; Ding, D.; Pu, K., Amphiphilic Semiconducting Polymer as Multifunctional Nanocarrier for Fluorescence/Photoacoustic Imaging Guided Chemo-Photothermal Therapy. *Biomaterials* **2017**, *145*, 168-177.

- (20) Zhu, H.; Fang, Y.; Miao, Q.; Qi, X.; Ding, D.; Chen, P.; Pu, K., Regulating Near-Infrared Photodynamic Properties of Semiconducting Polymer Nanotheranostics for Optimized Cancer Therapy. *ACS Nano* **2017**, *11*, 8998-9009.
- (21) Lyu, Y.; Fang, Y.; Miao, Q.; Zhen, X.; Ding, D.; Pu, K., Intraparticle Molecular Orbital Engineering of Semiconducting Polymer Nanoparticles as Amplified Theranostics for *in Vivo* Photoacoustic Imaging and Photothermal Therapy. *ACS Nano* **2016**, *10*, 4472-4481.
- (22) Lyu, Y.; Cui, D.; Sun, H.; Miao, Y.; Duan, H.; Pu, K., Dendronized Semiconducting Polymer as Photothermal Nanocarrier for Remote Activation of Gene Expression. *Angew. Chem., Int. Ed.* **2017**, *56*, 9155-9159.
- (23) Li, J.; Xie, C.; Huang, J.; Jiang, Y.; Miao, Q.; Pu, K., Semiconducting Polymer Nanoenzymes with Photothermic Activity for Enhanced Cancer Therapy. *Angew. Chem., Int. Ed.* **2018**, *57*, 3995-3998.
- (24) Yi, X.; Yang, K.; Liang, C.; Zhong, X. Y.; Ning, P.; Song, G. S.; Wang, D. L.; Ge, C. C.; Chen, C. Y.; Chai, Z. F.; Liu, Z. Imaging-Guided Combined Photothermal and Radiotherapy to Treat Subcutaneous and Metastatic Tumors Using Iodine-<sup>131</sup>-Doped Copper Sulfide Nanoparticles. *Adv. Funct. Mater.* **2015**, *25*, 4689-4699.
- (25) Cheng, X. J.; Yong, Y.; Dai, Y. H.; Song, X.; Yang, G.; Pan, Y.; Ge, C. C. Enhanced Radiotherapy Using Bismuth Sulfide Nanoagents Combined with Photothermal Treatment. *Theranostics* **2017**, *7*, 4087-4098.
- (26) Jiang, W.; Tang, C.; Chang, J. Y. Radiation with Immunotherapy: an Emerging Combination for Cancer Treatment. *J. Radiat. Oncol.* **2015**, *4*, 331-338.
- (27) Cooper, D. R.; Bekah, D.; Nadeau, J. L. Gold Nanoparticles and Their Alternatives for Radiation Therapy Enhancement. *Front. Chem.* **2014**, *2*, 1-13.
- (28) Fan, W. P.; Shen, B.; Bu, W. B.; Chen, F.; Zhao, K. L.; Zhang, S. J.; Zhou, L. P.; Peng, W. J.; Xiao, Q. F.; Xing, H. Y.; Liu, J. N.; Ni, D. L.; He, Q. J.; Shi, J. L. Rattle-Structured Multifunctional Nanotheranostics for Synergetic Chemo-/Radiotherapy and Simultaneous Magnetic/Luminescent Dual-Mode Imaging. *J. Am. Chem. Soc.* **2013**, *135*, 6494-6503.

- (29) Setua, S.; Ouberaï, M.; Piccirillo, S. G.; Watts, C.; Welland, M. Cisplatin-Tethered Gold Nanospheres for Multimodal Chemo-Radiotherapy of Glioblastoma. *Nanoscale* **2014**, *6*, 10865-10873.
- (30) Ma, M.; Huang, Y.; Chen, H. R.; Jia, X. Q.; Wang, S. G.; Wang, Z. Z.; Shi, J. L. Bi<sub>2</sub>S<sub>3</sub>-Embedded Mesoporous Silica Nanoparticles for Efficient Drug Delivery and Interstitial Radiotherapy Sensitization. *Biomaterials* **2015**, *37*, 447-455.
- (31) Yong, Y.; Cheng, X. J.; Bao, T.; Zu, M.; Yan, L.; Yin, W. Y.; Ge, C. C.; Wang, D. L.; Gu, Z. J.; Zhao, Y. L. Tungsten Sulfide Quantum Dots as Multifunctional Nanotheranostics for *in Vivo* Dual-Modal Image-Guided Photothermal/Radiotherapy Synergistic Therapy. *ACS Nano* **2015**, *9*, 12451-12463.
- (32) Zhang, S. H.; Sun, C. X.; Zeng, J. F.; Sun, Q.; Wang, G. L.; Wang, Y.; Wu, Y.; Dou, S. X.; Gao, M. Y.; Li, Z. Ambient Aqueous Synthesis of Ultrasmall PEGylated Cu<sub>2-x</sub>Se Nanoparticles as a Multifunctional Theranostic Agent for Multimodal Imaging Guided Photothermal Therapy of Cancer. *Adv. Mater.* **2016**, *28*, 8927-8936.
- (33) Jiang, X. X.; Zhang, S. H.; Ren, F.; Chen, L.; Zeng, J. F.; Zhu, M.; Cheng, Z. X.; Gao, M. Y.; Li, Z. Ultrasmall Magnetic CuFeSe<sub>2</sub> Ternary Nanocrystals for Multimodal Imaging Guided Photothermal Therapy of Cancer. *ACS Nano* **2017**, *11*, 5633-5645.
- (34) Jiang, X. X.; Han, Y. B.; Zhang, H.; Liu, H. H.; Huang, Q.; Wang, T. T.; Sun, Q.; Li, Z. Cu-Fe-Se Ternary Nanosheet-Based Drug Delivery Carrier for Multimodal Imaging and Combined Chemo-photothermal Therapy of Cancer. *ACS Appl. Mater. Interfaces* **2018**, *10*, 43396-43404.
- (35) Sun, C. X.; Xu, Y. F.; Deng, L. J.; Zhang, H.; Sun, Q.; Zhao, C. J.; Li, Z. Blood Circulation, Biodistribution, and Pharmacokinetics of Dextran-Modified Black Phosphorus Nanoparticles. *ACS Appl. Bio Mater.* **2018**, *1*, 673-682.
- (36) Sun, S.; Li, P.; Liang, S.; Yang, Z. Diversified Copper Sulfide (Cu<sub>2-x</sub>S) Micro-Nanostructures: a Comprehensive Review on Synthesis, Modifications and Applications. *Nanoscale* **2017**, *9*, 11357-11404.
- (37) Zhang, H.; Wang, T. T.; Qiu, W. B.; Han, Y. B.; Sun, Q.; Zeng, J. F.; Yan, F.; Zheng, H. R.; Li, Z.; Gao, M. Y. Monitoring the Opening and Recovery of the Blood–

Brain Barrier with Noninvasive Molecular Imaging by Biodegradable Ultrasmall Cu<sub>2-x</sub>Se Nanoparticles. *Nano Lett.* **2018**, *18*, 4985-4992.

(38) Sun, C. X.; Wen, L.; Zeng, J. F.; Wang, Y.; Sun, Q.; Deng, L. J.; Zhao, C. J.; Li, Z. One-Pot Solventless Preparation of PEGylated Black Phosphorus Nanoparticles for Photoacoustic Imaging and Photothermal Therapy of Cancer. *Biomaterials* **2016**, *91*, 81-89.

(39) Deng, L. J.; Xu, Y. F.; Sun, C. X.; Yun, B. F.; Sun, Q.; Zhao, C. J.; Li, Z. Functionalization of Small Black Phosphorus Nanoparticles for Targeted Imaging and Photothermal Therapy of Cancer. *Sci. Bull.* **2018**, *63*, 917-924.

(40) Liu, H. H.; Ren, F.; Zhang, H.; Han, Y. B.; Qin, H. Z.; Zeng, J. F.; Wang, Y.; Sun, Q.; Li, Z.; Gao, M. Y. Oral Administration of Highly Bright Cr<sup>3+</sup> Doped ZnGa<sub>2</sub>O<sub>4</sub> Nanocrystals for *in Vivo* Targeted Imaging of Orthotopic Breast Cancer. *J. Mater. Chem. B.* **2018**, *6*, 1508-1518.

(41) Motl, N. E.; Bondi, J. F.; Schaak, R. E. Synthesis of Colloidal Au–Cu<sub>2</sub>S Heterodimers *via* Chemically Triggered Phase Segregation of AuCu Nanoparticles. *Chem. Mater.* **2012**, *24*, 1552-1554.

(42) Fenton, J. L.; Steimle, B. C.; Schaak, R. E. Tunable Intraparticle Frameworks for Creating Complex Heterostructured Nanoparticle Libraries. *Science* **2018**, *360*, 513-517.

(43) Zhu, H.; Wang, Y.; Chen, C.; Ma, M. R.; Zeng, J. F.; Li, S. Z.; Xia, Y. S.; Gao, M. Y. Monodisperse Dual Plasmonic Au@Cu<sub>2-x</sub>E (E= S, Se) Core@Shell Supraparticles: Aqueous Fabrication, Multimodal Imaging, and Tumor Therapy at *in Vivo* Level. *ACS Nano* **2017**, *11*, 8273-8281.

(44) Ji, M.; Xu, M.; Zhang, W.; Yang, Z.; Huang, L.; Liu, J.; Zhang, Y.; Gu, L.; Yu, Y.; Hao, W.; An, P.; Zheng, L.; Zhu, H.; Zhang, J. Structurally Well-Defined Au@Cu<sub>2-x</sub>S Core-Shell Nanocrystals for Improved Cancer Treatment Based on Enhanced Photothermal Efficiency. *Adv. Mater.* **2016**, *28*, 3094-3101.

(45) Ding, X.; Liow, C. H.; Zhang, M.; Huang, R.; Li, C.; Shen, H.; Liu, M.; Zou, Y.; Gao, N.; Zhang, Z.; Li, Y.; Wang, Q.; Li, S.; Jiang, J. Surface Plasmon Resonance

Enhanced Light Absorption and Photothermal Therapy in the Second Near-Infrared Window. *J. Am. Chem. Soc.* **2014**, *136*, 15684-93.

(46) Cui, J.; Jiang, R.; Guo, C.; Bai, X.; Xu, S.; Wang, L. Fluorine Grafted Cu<sub>7</sub>S<sub>4</sub>-Au Heterodimers for Multimodal Imaging Guided Photothermal Therapy with High Penetration Depth. *J. Am. Chem. Soc.* **2018**, *140*, 5890-5894.

(47) Wolf, A.; Kodanek, T.; Dorfs, D. Tuning the LSPR in Copper Chalcogenide Nanoparticles by Cation Intercalation, Cation Exchange and Metal Growth. *Nanoscale* **2015**, *7*, 19519-19527.

(48) Zhu, D. W.; Liu, M. X.; Liu, X.; Liu, Y.; Prasad, P. N.; Swihart, M. T. Au-Cu<sub>2-x</sub>Se Heterogeneous Nanocrystals for Efficient Photothermal Heating for Cancer Therapy. *J. Mater. Chem. B.* **2017**, *5*, 4934-4942.

(49) Liu, X.; Lee, C.; Law, W. C.; Zhu, D.; Liu, M.; Jeon, M.; Kim, J.; Prasad, P. N.; Kim, C.; Swihart, M. T. Au-Cu<sub>2-x</sub>Se Heterodimer Nanoparticles with Broad Localized Surface Plasmon Resonance as Contrast Agents for Deep Tissue Imaging. *Nano Lett.* **2013**, *13*, 4333-4339.

(50) Hu, C.; Chen, W.; Xie, Y.; Verma, S. K.; Destro, P.; Zhan, G.; Chen, X.; Zhao, X.; Schuck, P. J.; Kriegel, I.; Manna, L. Generating Plasmonic Heterostructures by Cation Exchange and Redox Reactions of Covellite CuS Nanocrystals with Au<sup>3+</sup> Ions. *Nanoscale* **2018**, *10*, 2781-2789.

(51) Lie, S. Q.; Wang, D. M.; Gao, M. X.; Huang, C. Z. Controllable Copper Deficiency in Cu<sub>2-x</sub>Se Nanocrystals with Tunable Localized Surface Plasmon Resonance and Enhanced Chemiluminescence. *Nanoscale* **2014**, *6*, 10289-10296.

(52) Zhang, S. H.; Huang, Q.; Zhang, L. J.; Zhang, H.; Han, Y. B.; Sun, Q.; Cheng, Z. X.; Qin, H. Z.; Dou, S. X.; Li, Z. Vacancy Engineering of Cu<sub>2-x</sub>Se Nanoparticles with Tunable LSPR and Magnetism for Dual-Modal Imaging Guided Photothermal Therapy of Cancer. *Nanoscale* **2018**, *10*, 3130-3143.

(53) Louie, A. Multimodality Imaging Probes: Design and Challenges. *Chem. Rev.* **2010**, *110*, 3146-3195.

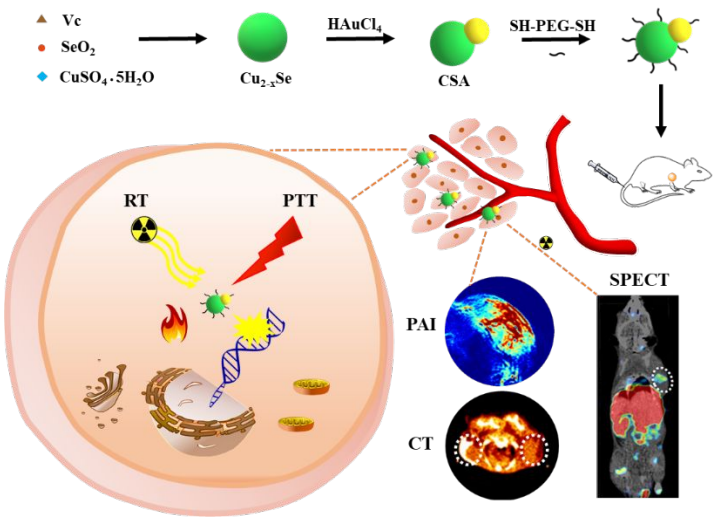
(54) Kunzmann, A.; Andersson, B.; Thurnherr, T.; Krug, H.; Scheynius, A.; Fadeel, B.

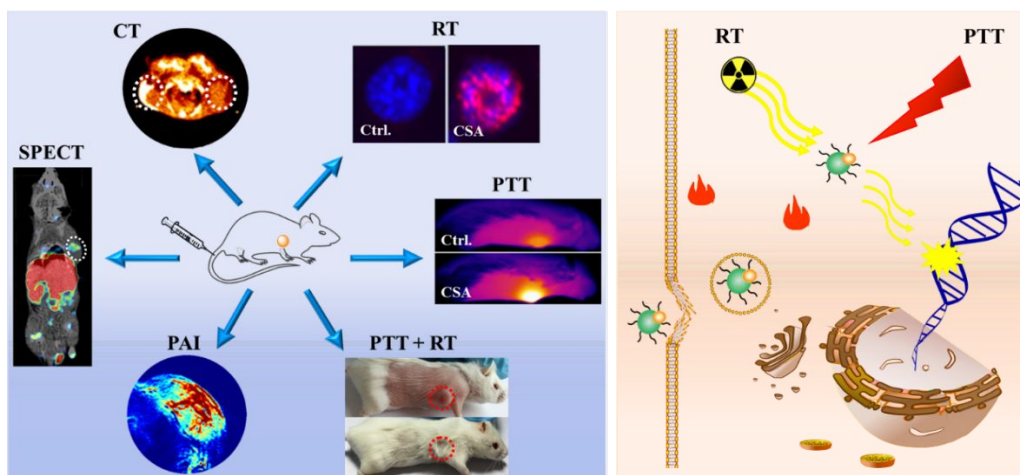


1  
2  
3  
4 Toxicology of Engineered Nanomaterials: Focus on Biocompatibility, Biodistribution  
5 and Biodegradation. *Biochim. Biophys. Acta, Gen. Subj.* **2011**, *1810*, 361-373.

6  
7  
8 (55) Chang, Y. Z.; He, L. Z.; Li, Z. B.; Zeng, L. L.; Song, Z. H.; Li, P. H.; Chan, L.;  
9 You, Y. Y.; Yu, X. F.; Chu, P. K.; Chen, T. F. Designing Core–Shell Gold and Selenium  
10 Nanocomposites for Cancer Radiochemotherapy. *ACS Nano* **2017**, *11*, 4848-4858.  
11  
12  
13  
14  
15  
16  
17  
18  
19  
20  
21  
22  
23  
24  
25  
26  
27  
28  
29  
30  
31  
32  
33  
34  
35  
36  
37  
38  
39  
40  
41  
42  
43  
44  
45  
46  
47  
48  
49  
50  
51  
52  
53  
54  
55  
56  
57  
58  
59  
60

TOC:





**Scheme 1.** The application (left) and mechanism (right) of heterogeneous CSA nanoparticles for PA/SPECT/CT multimodal imaging and synergistic radiophotothermal therapy of cancer.

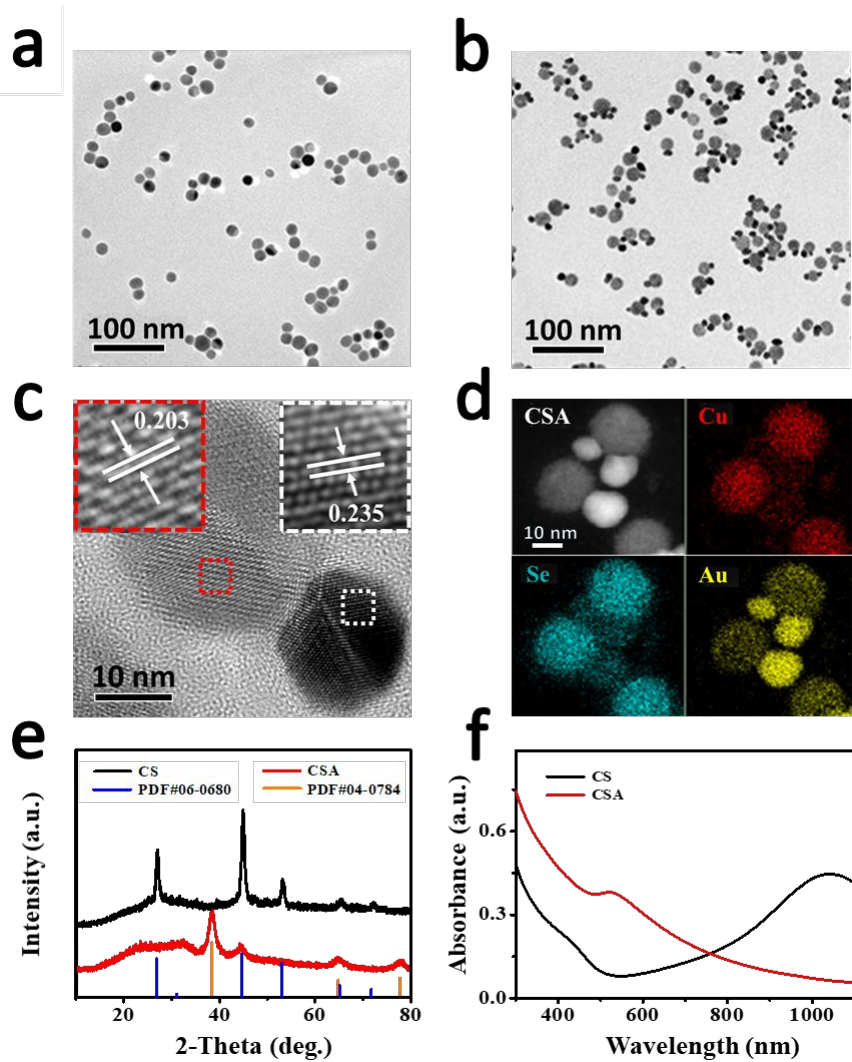


**Figure 1.** TEM images of (a) CS and (b) CSA nanoparticles, (c) HRTEM image with magnified lattice fringes shown in the insets, (d) high-angle annular dark-field-scanning TEM (HAADF-STEM) EDS elemental mapping images of CSA nanoparticles, (e) XRD patterns of CS and CSA nanoparticles (PDF#06-0680: Cu<sub>2-x</sub>Se, PDF#04-0784: Au), (f) UV absorbance spectra of CS (black) and CSA (red) nanoparticles.

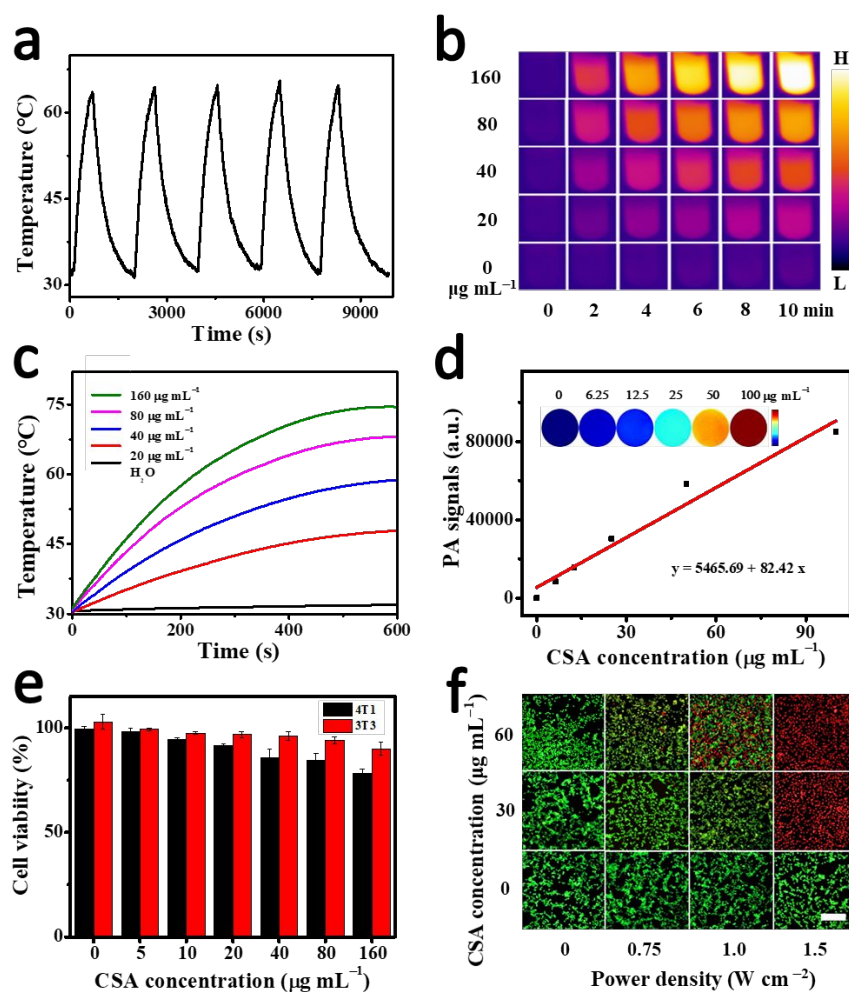


**Figure 2.** (a) Photothermal stability of a CSA solution over five cycles of heating/cooling processes in which the heating was performed by irradiation with a 808-nm NIR laser ( $0.75 \text{ W cm}^{-2}$ ), (b) photographs and (c) photothermal heating curves of CSA solutions in different concentrations (*i.e.* 0, 20, 40, 80, and  $160 \mu\text{g mL}^{-1}$ ) irradiated by an 808 nm laser ( $0.75 \text{ W cm}^{-2}$ , 10 min), (d) *in vitro* PA images and signals of CSA solutions in different concentrations under excitation by 680 nm light, (e) *in vitro* cytotoxicity of different concentrations of CSA nanoparticles to 4T1 cells and 3T3 cells, (f) live/dead images of 4T1 cells after they were cultured with CSA nanoparticles in concentrations of 0, 30, and  $60 \mu\text{g mL}^{-1}$  and irradiated with an 808 nm laser for 5 min with a power density of 0, 0.75, 1, and  $1.5 \text{ W cm}^{-2}$ , respectively.

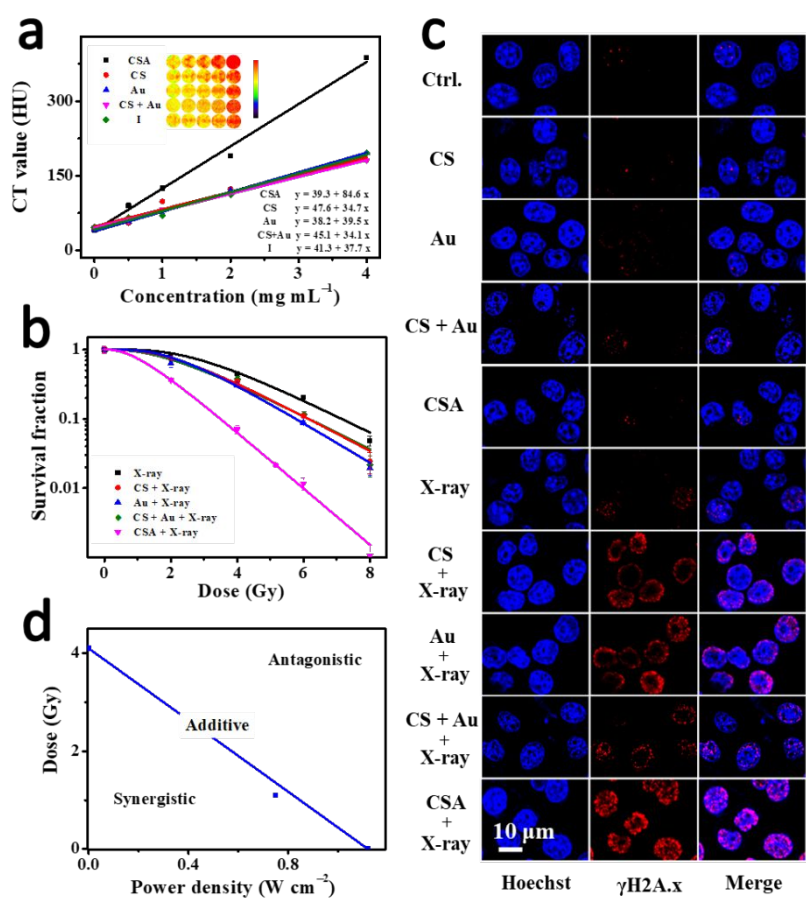


**Figure 3.** (a) *In vitro* CT images and signal intensities of CSA nanoparticles in comparison with CS, Au, CS + Au nanoparticles and commercially used iopromide in different concentrations, (b) survival rates of 4T1 cells treated with/without CS, Au, CS + Au and CSA nanoparticles ( $60 \mu\text{g mL}^{-1}$ ) under different doses of X-rays (*i.e.*, 0, 2, 4, 6, and 8 Gy), (c) DNA damage to 4T1 cells irradiated with 6 Gy X-rays in the presence or absence of CS, Au, CS + Au and CSA nanoparticles ( $60 \mu\text{g mL}^{-1}$ ), (d) isobologram analysis of the synergistic antiproliferative effect of laser and X-rays applied to 4T1 cells after cultured with CSA nanoparticles. The data points in the isobologram correspond to the growth inhibition ratio at 50% in the combined treatment.

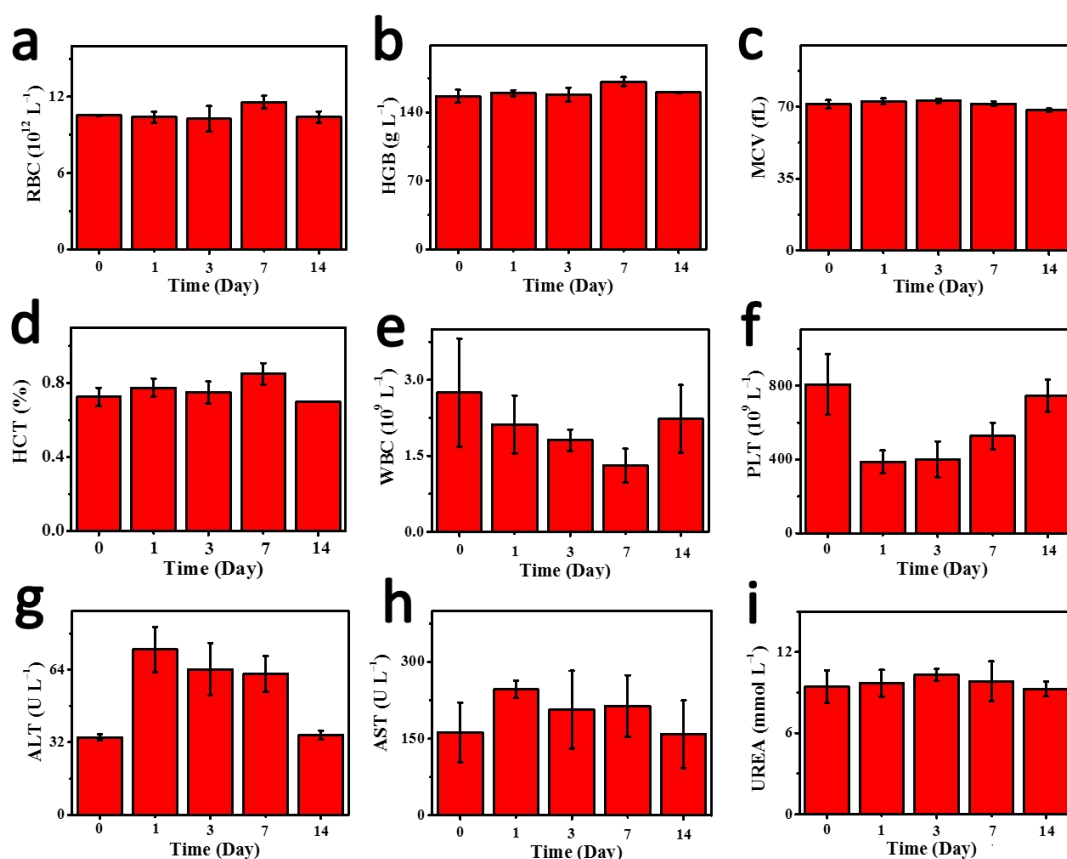


**Figure 4.** Blood routine examination of (a) red blood cells (RBC), (b) hemoglobin (HGB), (c) mean corpuscular volume (MCV), and (d) hematocrit (HCT), (e) white blood cells (WBC), (f) platelets (PLT) after the mice were injected with CSA nanoparticles. Blood biochemistry analyses of (g) alanine aminotransferase (ALT), (h) aspartate aminotransferase (AST), and (i) urea nitrogen (UREA) from the mice injected with CSA nanoparticles. The injected dose of CSA nanoparticles was  $25 \text{ mg kg}^{-1}$ . All the indicators were also examined from four mice without injection of CSA nanoparticles and used as a reference.



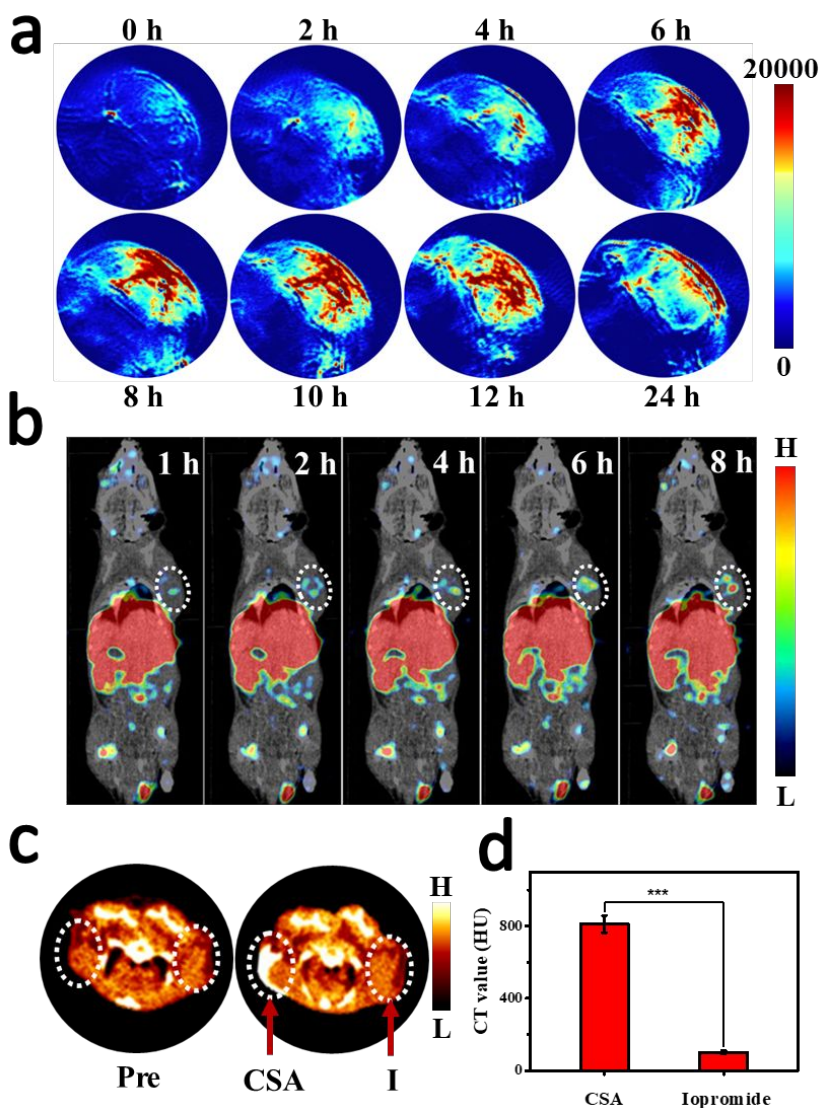


**Figure 5.** (a) *In vivo* PA images of tumor acquired before and after intravenous injection of PEGylated CSA solution ( $2.5 \text{ mg mL}^{-1}$ ,  $200 \text{ }\mu\text{L}$ ) into a mouse bearing a 4T1 tumor, (b) *in vivo* SPECT/CT images of a 4T1 tumor-bearing mouse obtained at different times post injection of  $^{99\text{m}}\text{Tc}$  labeled CSA nanoparticle solution, (c) *in vivo* CT images and (d) signal intensities of 4T1 tumors after intratumoral injection of CSA nanoparticles (left) and iopromide solution (right) with the same dose of  $30 \text{ mg kg}^{-1}$  (\* $p < 0.05$ , \*\* $p < 0.001$ , \*\*\* $p < 0.0001$ ).



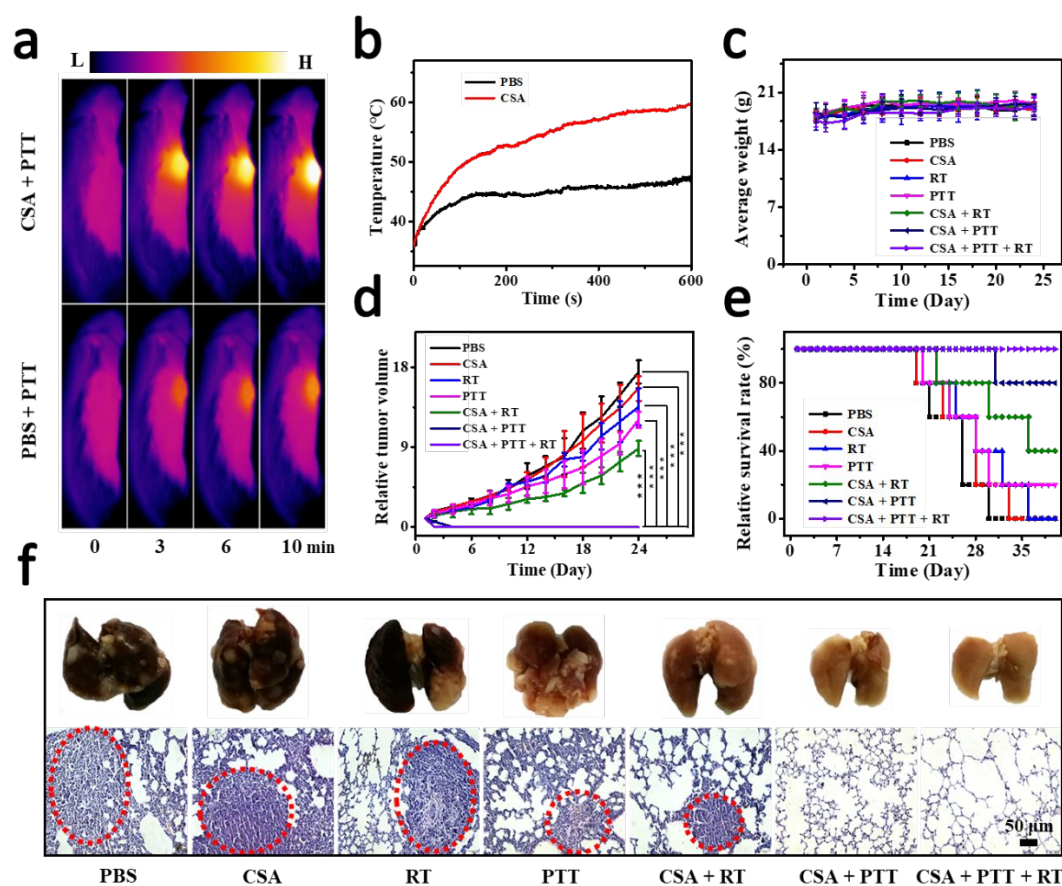


**Figure 6.** (a) Infrared thermal images of tumor-bearing mice and (b) the temperature curves of the tumor site after they were intravenously injected with CSA nanoparticles (dose  $2.5 \text{ mg mL}^{-1}$ ,  $200 \mu\text{L}$ ) and PBS, respectively, and then exposed to an 808 nm NIR laser ( $1.5 \text{ W cm}^{-2}$ , 10 min); the variations in (c) weight, (d) relative tumor volume, and (e) survival rates of mice from the different groups treated under different conditions; (f) images of whole lungs of mice collected from different groups at the end of treatment (top), and the corresponding lung slices stained with hematoxylin and eosin (H&E) (bottom). (\* $p < 0.05$ , \*\* $p < 0.001$ , \*\*\* $p < 0.0001$ )